Magneto-Optical Trapping and Control for a Neutral Atom Quantum Computer

Buke Hu

A thesis
submitted in partial fulfillment of the
requirements for the degree of

Master of Science

University of Washington

2025

Reading Committee:

Maxwell Parsons, Chair

Sara Mouradian

Program Authorized to Offer Degree:
UW Electrical and Computer Engineering

University of Washington

Abstract

Magneto-Optical Trapping and Control for a Neutral Atom Quantum Computer

Buke Hu

Chair of the Supervisory Committee:
Maxwell Parsons
Electrical and Computer Engineering

This thesis presents the design, implementation, and characterization of a Rubidium-87 Magneto-Optical Trap (MOT) developed as a part of the foundation of a neutral atom quantum computing platform. A two-dimensional (2D) MOT and a 2D+ MOT configuration are realized to generate and deliver a cold atomic beam for future three-dimensional trapping.

The experimental system integrates laser locking based on saturated absorption spectroscopy, radio-frequency control of acousto-optic and electro-optic modulators, permanent-magnet field generation, and a real-time FPGA-based control system. The 2D MOT is characterized using fluorescence imaging, and the 2D+ atomic beam is characterized by transversal probe beam spectroscopy. We extract the linewidth and assess Doppler and power-broadening effects.

The results demonstrate stable generation of a collimated atomic beam and establish a robust testbed for future integration with optical tweezers and scalable neutral atom quantum computing architectures.

TABLE OF CONTENTS

LIST OF FIGURES

Figure Number Page

ACKNOWLEDGMENTS

I would like to express my sincere gratitude to **Max Parsons** for his guidance, support, and insight throughout this research. His mentorship was essential to the development of this work.

I would also like to thank my committee member, **Sara Mouradian**, for her valuable feedback and thoughtful discussions.

I am grateful to the members of **Parsons Lab**, especially **Ohik Kwon** and **Kevin Wu**, for their technical assistance, collaboration, and for creating a supportive research environment.

DEDICATION

This thesis is dedicated to the members of Parsons Lab, my family, my friends, and those who supported me throughout this journey.

Chapter 1

INTRODUCTION

Quantum computing promises substantial advancements in computational capability, as demonstrated by recent progress in academia and industry. Classical bit-based computing has reshaped the world since the mid-20th century. It builds an interconnected human society. Most people have easier access to information and technology. It provides extraordinary reliability and flexibility for many classical problems while maintaining low power consumption and high processing speed. Automation and control, data processing, and daily information presentation are examples of how classical computation significantly helps people. However, classical computers have also encountered problems that cannot be solved in a reasonable time. Quantum computers can provide some speedup for specific problems, and the range of that specific problem list is still increasing.

With 74 algorithms currently listed in the Quantum Algorithm Zoo [1], each can provide a different speedup for various cases. The quantum search algorithm, also known as Grover's algorithm [2], is a famous quantum algorithm. By iteratively applying a unitary operation

$$G = H^{\otimes n} Z_{or} H^{\otimes n} Z_f \tag{1.1}$$

to a prepared n-qubit quantum register in the $|+\rangle$ state [3], Grover's algorithm can find the target with a time complexity of $O(\sqrt{N})$, a quadratic speedup compared to the classical linear search algorithm, which has a time complexity of $O(N)$ for unstructured search. The Quantum Approximate Optimization Algorithm (QAOA) is another quantum algorithm famous for optimizing combinatorial optimization problems [4]. Many scientific applications, such as the simulation of molecular systems, could benefit from the QAOA algorithm. We may also use it to optimize the Traveling Salesman Problem.

Another example, where a quantum algorithm provides an exponential speedup over the classical solution, is the analysis of electrical resistance in an interconnected resistor network [5]. This algorithm achieves $O(log\ N)$ complexity, where N is the number of vertices (nodes between resistors) in the network, exponentially faster than the classical $O(N)$ solution. This very practical algorithm can calculate the effective resistance between any two points in this given network and can also be used to improve some algorithms related to graph [5].

Such algorithms demonstrate the remarkable potential of quantum computing; however, it is important to remember that practical implementation remains constrained by today's hardware realities.

In the NISQ era, while algorithmic innovation lays the theoretical foundation for quantum advantage, we still need hardware, control electronics, error-correction protocols, and software infrastructure that ultimately determine how these algorithms can run in practice to become true applications [6].

1.1 Quantum Hardware

For quantum hardware platforms, many research groups and commercial companies have made significant progress in producing high-fidelity, reliable quantum computing platforms. Here are some popular technical routes in the quantum hardware industry:

- **Superconducting Qubits:** Superconducting qubits encode information in the discrete energy levels of Josephson-junction circuits. They operate at 10–100 mK in dilution refrigerators, enabling rapid gate times of about 50 ns, and >99% single- and two-qubit fidelities demonstrated by Barends et al. in 2014 [7]. With coherence times reaching up to 1.48 ms [8], one can perform gate operations on the order of 10^4 per coherence window due to limitations caused by dielectric losses and quasi-particle poisoning. The reliance on bulky dilution refrigerators and extensive wiring harnesses presents serious engineering bottlenecks for large-scale integration [9]. Despite these challenges, major companies like Google (which claimed quantum supremacy in 2019 [10]), Rigetti, IBM, and Quantinuum have all invested heavily in superconducting platforms.

- **Trapped-Ion Qubits:** Trapped-ion qubits encode information in the electronic states of individual atomic ions confined in electric field traps under ultrahigh vacuum (UHV)

[11]. In such an isolated environment, particles are well shielded from environmental noise, enabling higher operation fidelities than most solid state quantum devices: single-qubit gate error rates as low as $3 * 10^{-5}$ and two-qubit gate error rates around $2 * 10^{-3}$ have been demonstrated [12]. Scalability remains a major challenge due to trap size, control complexity, and crosstalk between particles. Proposed solutions include the Quantum Charge-Coupled Device (QCCD) architecture, where ions are shuttled between interconnected trap zones [13], and modular designs that link multiple ion-trap modules via photonic interconnects [14]. These approaches aim to preserve UHV isolation while extending system size. Commercial players have also entered the trapped-ion arena: IonQ, for example, offers cloud-accessible trapped-ion processors (e.g., IonQ Aria) that harness this technology for both research and industry applications [15, 16]. Their systems currently support tens of qubits, with roadmap plans for scaling through improved trap designs and modular interconnects.

- **Photonic Qubits:** Photons are usually used as intermediates in other platforms because they have high speed, low decoherence, and can be generated from atomic transitions [17], but it is also possible to use photons to perform quantum computing directly [18]. People choose to encode information in the polarization, path, time-bin, or spatial mode [19]. These methods allow a high level of isolation from the environment without UHV, as photons do not interact with each other very often. With the recent development of photonic integrated circuit (PIC) technologies, miniaturization is also possible [20]. The proximity of photons to communication allows for scaling by interconnecting multiple devices. However, photonic quantum gates suffer from a relatively low two-qubit entangling rate. Achieving high-fidelity gates requires significant overhead (auxiliary photons, multiplexing) [21]. Companies like PsiQuantum and Xanadu chose this route and have made significant progress in scaling and error correction [22, 23].

- **Spin Qubits:** Spin qubits are a class of solid-state quantum bits in which information is stored in the spin degree of freedom of a charge carrier, examples include defect centers in diamond and electrons trapped in silicon dots. In the specific realm of semiconductor spin qubits, there are four main modalities: single-spin qubits, donor-spin qubits, singlet–triplet qubits, and exchange-only qubits [24]. Because silicon-based spin devices can be fabricated using lithography, doping, and thin-film processes, they benefit from mature microelectronics equipment [25]; however, they still demand atomic-scale placement accuracy, ultra-clean interfaces, and specialized cryogenic packaging. State-of-the-art silicon spin qubits now achieve single-qubit gate fidelities of up to 99.99% [26] and two-qubit fidelities exceeding 98.9% [27]. To reach these performance levels, devices operate in cryogenic environments that suppress thermal and charge noise. However, most demonstrations to date involve only a small number of qubits (a two-qubit processor in the previous example), which highlights the significant challenge of scaling these solid-state devices to larger systems.

- **Neutral Atom Qubits:** Neutral atom systems store quantum information in the hyperfine ground states of electrically neutral atoms, such as rubidium or cesium. Such atoms are individually trapped with tightly focused optical tweezers or arranged in optical lattices under ultrahigh vacuum. Unlike charged ions, neutral atoms do not experience mutual Coulomb repulsion, thus allowing for dense packing and highly scalable architectures. Arrays with more than 6100 qubits have successfully replicated just recently [28]. The neutral atom platform has several advantages: long coherence time (T_1 on the order of seconds and T_2 of up to hundreds of milliseconds), minimal crosstalk between qubits, and high scalability. The current limitation of this platform is mainly the rearrangement efficiency for large arrays and the finite lifetime of the Rydberg state of the atom [29]. Companies such as QuEra, Atom Computing, and PASQAL are actively developing commercial neutral atom quantum computers, offering the industry early access to scalable quantum hardware and applications [30, 31].

1.2 Overview about Neutral Atoms Quantum Computing

1.2.1 Rydberg Blockade

Rydberg Blockade is a very important phenomenon when entangling neutral atom quantum computers. In some special atoms, such as Rubidium, coherent laser excitation can move a ground-state atom to a highly excited Rydberg state $|r\rangle$, where the principal quantum number for this Rydberg state is $n \gg 1$. If one atom is excited to a Rydberg state, then exciting a second nearby atom is off-resonant because the $|rr\rangle$ state is shifted by B. When the interaction-induced shift exceeds the single-atom Rabi frequency, $B \gg \Omega$, the second atom will be suppressed within a characteristic blockade radius R_b, typically a few micrometers for the $n \approx 60$–100 states used in experiments. Thus, the second atom can never reach the Rydberg state in the ideal case, until the first atom falls out of the Rydberg state. In this regime, only one collective Rydberg excitation is allowed inside the blockade volume.

Two-qubit entangling gates in neutral atoms utilize this phenomenon. A standard CZ or $CNOT$ gate sequence applies a π pulse on the control qubit to drive $|1\rangle \to |r\rangle$, followed by a 2π pulse on the target qubit, and a final π pulse returning the control from $|r\rangle \to |1\rangle$. If the control is initially in $|1\rangle$, its excitation to $|r\rangle$ blockades the target, so the 2π pulse only adds a dynamical phase; if the control is in $|0\rangle$, the target undergoes a full Rabi cycle [32]. The differential phase between these cases implements a controlled phase gate, which can be converted to a CNOT with single-qubit rotations. This protocol generalizes naturally to multi-qubit blockade, enabling collective gates, GHZ-state preparation, and native multi-controlled operations that are difficult to realize in other platforms [33, 32].

But this does not promise 100% fidelity. The energy shift B is not infinite. Depending on the distance between atoms, the specific Rydberg state used, and the orientation of the atomic dipoles, leakage into the doubly excited state $|rr\rangle$ can occur, causing imperfect blockade and, thus, gate errors. Atoms in the Rydberg energy levels also have a much shorter lifetime than their ground states, leading to more likely decay and dephasing during the gate operation.

1.2.2 Technology Paths

Among the various quantum hardware platforms, neutral atom systems stand out for their scalability and commercial potential. They have demonstrated high-fidelity two-qubit gate operations [34] and can operate at room temperature. The fidelity still remains high without the bulky dilution refrigerators isolating the environment. This simplifies system engineering, allowing for more complex work around the vacuum. Flexible, all-to-all connectivity has been achieved by repositioning atoms with AOD tweezers [35], and their long coherence times further strengthen their case as a leading candidate for large-scale, fault-tolerant quantum computing.

There are different technological pathways for neutral atom quantum computing, differentiated by their choices of atoms and information encoding schemes.

- Alkali Rydberg Atoms (e.g., Rb, Cs): Qubits encode information in the hyperfine energy levels, using the long range Rydberg effect to interact with one another, as mentioned in subsection 1.2.1.

- Alkaline-Earth Atoms (e.g., Sr, Yb): Qubits encode information in the optical "clock" state. Interactions are usually made through alkaline-earth Rydberg states or spin-exchange mechanisms [36].

- Dipolar Particles (polar molecules / dipolar atoms): These types of particles are also electrically neutral and have similar control methods, so they are considered to be neutral "atoms" as well. They encode information in the internal (spin/rotation) state of dipolar particles, using long range electric or magnetic dipole-dipole interactions to achieve multi-qubit gates[37].

Alkali atoms form a leading quantum computing platform. Mark Saffman's group achieved the first two-qubit gate with neutral atoms in 2010 [38]. Mikhail Lukin's group has pushed the scale of these systems: they built a 51-qubit programmable Rydberg simulator in 2017 and later a 256-qubit array in 2021, observing exotic quantum phases in large atom grids [39, 40]. Recent advances have dramatically improved gate fidelity. They achieved

99.5% fidelity with two-qubit Rydberg gates applied in parallel across 60 atoms, surpassing error-correction thresholds. Also, Lukin's group realized the first logical qubit implementation on Rydberg atoms [41]. These milestones underscore the alkali-atom path's rapid progress in both system size and reliable quantum logic.

Another path is the Alkaline-Earth atoms, such as Ytterbium and Strontium. On this type of platform, information is usually encoded in the nuclear spin state [36]. These atoms have ultra-narrow optical transitions and long-lived metastable states, allowing qubits to be encoded with superior coherence and stability. These properties also make them promising for neutral-atom quantum computing architectures, as they support optical qubits and hybrid schemes that are complementary to the fast Rydberg-based gates of alkali atoms [42]. Manuel Endres's team at Caltech showed in 2020 that two strontium-88 atoms in optical tweezers could be entangled via Rydberg excitation with record fidelity [43]. And they broke the record for the largest tweezer array size in 2025, reaching an astonishing 6100 individually trapped atoms [28].

The third path is the dipolar particle path. In this quantum computing path, qubits interact with each other through dipole–dipole forces. David DeMille in 2001 proposed using molecules to achieves this [44]. Kang-Kuen Ni's group from Harvard recently achieved a landmark result: they trapped ultra-cold NaCs molecules in optical tweezers and implemented the first universal two-qubit gate between individually trapped NaCs polar molecules. They realized the iSWAP quantum gate that swapped the molecules' internal states and generated a two-qubit Bell state with about 94% fidelity [45]. Some other groups have explored magnetic atoms or different polar molecule species, e.g., Erbium [46]. The Ferlaino group from the University of Innsbruck achieved the first dipolar quantum mixture of highly magnetic erbium and dysprosium atoms, which could support next-generation multi-component qubits [46]. These approaches thus opened another promising route to scalable quantum processors.

1.2.3 Rubidium-87 as a Platform

We chose to use Rubidium 87 atoms as our platform. This choice allows us to build upon others' experiences. Many pieces of equipment were designed and optimized for this platform and frequency. As a result, we save considerable time and resources. The suitability of Rubidium 87 as a quantum computing platform can be evaluated using the five well-known DiVincenzo criteria for a universal quantum computer [47]. Multiple experimental demonstrations have shown that neutral atom systems meet all of these requirements [32], as outlined below:

- Well-defined qubits: Rubidium atoms have well-resolved energy levels. We choose the hyperfine ground states
  $|0\rangle = |F = 1, m_F = 0\rangle$ and
  $|1\rangle = |F = 2, m_F = 0\rangle$.
  to be our computational states. Both are long-lived energy levels.

- Initialization to a pure state: Before computation, we need to initialize our qubits to either $|0\rangle$ or $|1\rangle$. After all atoms are trapped, we can turn off the repump laser sideband, so all atoms fall into the dark state $|5^2S_{1/2}, F = 1, m_F = 0\rangle$, which would be $|0\rangle$.

- Universal set of quantum gates: Rydberg blockade enables quantum gate operation. [32]

- Qubit-specific measurement: To measure the state of an atomic qubit, we will shine D2 laser on the atoms and try to excite the atoms from $5^2S_{1/2}, F = 2$ to $5^2P_{3/2}, F' = 3$. If the target atom is in this state, it will emit a photon very shortly ($\tau = 26.2348$ ns. [48]) afterward due to spontaneous emission and fall back to the initial state, causing a cycling transition. We can capture the emitted photons from this cycling transition and identify the state of the qubit.

- Long Coherence Times: Neutral atoms are trapped in optical tweezers within ultra-high vacuum, minimizing collisional decoherence. With careful suppression of thermal and magnetic field fluctuations, coherence times on the order of seconds have been demonstrated. [32]

In alkali atoms quantum computing platform, single-qubit gates are typically implemented using either resonant microwave fields that directly drive transitions between the two hyperfine ground states ($F = 0$ and $F = 1$) [49], or by two-photon Raman transitions mediated by a detuned excited state [35]. Microwave radiation typically cannot be tightly focused to individual qubits due to its long wavelength. Raman transitions enable fast and spatially selective addressing when combined with tightly focused laser beams. Two-qubit gates are realized through strong, controllable interactions between atoms excited to high principal quantum number Rydberg states (see subsection 1.2.1) [35]. Gate fidelities above 99% have been reported in small-scale neutral atom systems, with performance primarily limited by Rydberg state decay, laser phase noise, and imperfect addressing [34].

1.3 Quantum Error Mitigation and Correction

Quantum computers have significantly more noise than classical computers. due to environmental decoherence, analog control signals, imperfections during manufacturing, cross-talk between qubits, and readout noise. The optimization of the key hardware components, such as the magneto-optical trap and associated laser cooling systems, can gradually improve the error rate as better methods continue to emerge. But beyond the hardware improvements, quantum error correction (QEC) provides a framework for protecting quantum information against noise by encoding logical qubits into multi-qubit entangled states and performing non-destructive syndrome measurements [50]. A well-designed QEC protocol can detect and correct both bit-flip and phase-flip errors without collapsing the encoded superposition, enabling reliable quantum computation once physical error rates fall below a threshold. 30 years after the first QEC code, more than 500 QEC codes are being studied [51]. Here are a few that have a major impact on the world with a brief introduction.

Stabilizer codes are a category of quantum error correction: a set of commuting “checks” (stabilizers) defines a protected subspace, and repeatedly measuring these checks reveals error syndromes without reading out the data itself [52, 53]. This formalism underpins most leading codes: Shor's [54], Steane [53], surface [55, 56], and color [57]. From a hardware perspective, these checks can be implemented with lower overhead and can be parallelized to improve efficiency. In practice, stabilizer codes offer local, low-weight parity checks, high thresholds with fast decoders, and fault-tolerant primitives (e.g., lattice surgery), giving clear engineering targets for fidelity, readout latency, and feedforward.

Other non-stabilizer codes—such as bosonic [58] or amplitude-damping codes [59]—are also being explored. However, stabilizer codes remain the dominant choice in both theory and experiment due to their mathematical tractability, efficient decoding algorithms, and compatibility with scalable hardware architectures. In neutral-atom platforms, significant recent milestones further underscore this trend: a demonstration on a 256-qubit neutral-atom processor showed the encoding of 24 logical qubits with error detection and correction of atom loss using surface code and color code [41]. Also in that experiment, surface codes (up to distance $d = 7$), color codes (up to 40 logical qubits), and three-dimensional $[8, 3, 2]$ code blocks (up to 48 logical qubits) were implemented with mid-circuit readout, lattice surgery, and multi-logical-gate operations [41]. These advances highlight the practical feasibility of fault-tolerant operations in neutral-atom systems, tightly aligning with hardware strengths such as flexible qubit placement, high-fidelity gates, and parallel readout.

Reaching such large-scale, fault-tolerant processors requires many challenging methods and technologies: holographic tweezers arrays to trap enough qubits in the system; atom rearrangement that moves individual atoms around to achieve all-to-all connectivity; and low phase noise lasers for entangling and gate operations. In this context, our lab is building a neutral atom testbed that is explicitly designed to explore new optical techniques for scalable architectures. The long-term goal is to realize three-dimensional atomic arrays using holographic imaging.

This thesis documents the early-stage engineering and experimental processes involved in constructing the neutral atom quantum computing platform based on Rubidium-87 atoms. Specifically, it focuses on the development and optimization of key components, such as the Magneto-Optical Trap (MOT) and associated laser cooling systems.

Chapter 2

MOT OVERVIEW AND THEORETICAL SUPPORT

2.1 What is MOT?

To confine and manipulate atoms in a vacuum chamber, physicists commonly use lasers and magnetic fields, as these offer precise and accurate control over phase, frequency, and timing without breaking the vacuum environment. In 1997, the Nobel Prize in Physics was awarded to Steven Chu, Claude Cohen-Tannoudji, and William D. Phillips for their pioneering contributions to the laser cooling and trapping of atoms [60]. Their work laid the foundation for the development of neutral atom quantum computing. The Magneto-Optical Trap (MOT) remains a standard tool in atomic physics and condensed matter research. The MOT enables the cooling and confinement of neutral atoms to micro-kelvin temperatures, allowing researchers to explore the behavior of matter in regimes close to absolute zero. Compared with alternatives such as purely magnetic traps or electrostatic Stark traps, MOTs are more flexible in terms of the types of particles and offer greater controllability.

In essence, the MOT uses a combination of six counter-propagating, circularly polarized laser beams and a magnetic field gradient produced by a pair of anti-Helmholtz coils. The magnetic field creates a position-dependent energy shift via the Zeeman effect, which, together with the optical forces from the lasers, provides both cooling and a restoring force toward the trap center.

In [61], Nosske *et al.* realized a transversely loaded 2D MOT for Strontium that acts as a high-flux cold atom source. Their 2D MOT captures atoms from a thermal beam, cools them in the transverse directions, and uses an additional pushing beam to form a slow, collimated atomic beam with tunable longitudinal velocity and a flux exceeding 10^9 atoms/s, which efficiently loads a downstream 3D MOT. In our experiment, we follow the same general strategy with ^{87}Rb: a $2D^+$ MOT captures and cools atoms in two dimensions and accelerates them toward a separate science chamber, where a 3D MOT provides full three-dimensional cooling and trapping. After sufficiently cooled in the 3D MOT, the atoms would remain clustered near the trap center. Then transferred into individually addressable optical tweezers for quantum computation.

The performance of the MOT can be analyzed using the following parameters: Temperature, density, loading rate, and capture velocity. The temperature reflects the residual kinetic energy in the atoms after cooling. Equivalently, temperature represents the average moving speed of the atoms and the average time an individual atom can survive in the atom array. The temperature strongly impacts coherence times and the error rate in the quantum computer. The atomic density describes the abundance of atoms in the MOT. With higher density, we could get stronger fluorescence, and vise versa. This property is limited by the reabsorption of scattered photons and light-assisted collisions. We can increase the atom density by tuning the magnetic field and optical setup using techniques such as compressed MOT or dark-spot MOT [62, 63]. The loading rate quantifies how fast MOT can capture atoms from the background vapor or atomic beam. It also determines how quickly the MOT reaches a steady state. This property depends on the background pressure, laser parameters, and loss rates [64]. Finally, the capture velocity is the maximum initial speed of an atom that can be decelerated and trapped by the MOT. It is determined by the detuning, intensity, beam size of the laser, and magnetic-field gradient. Balancing these parameters is critical for producing a MOT that can prepare us to build the neutral atom quantum computer.

We chose to use a 2D+ MOT as a cold atom source to load the 3D MOT. The advantages has been demonstrated in several experiments. In particular, [65] realized an intense cold ^{87}Rb beam based on a 2D+ MOT and characterized its performance in detail. We use this work as a useful benchmark for our 2D+ MOT system.

2.2 Theoretical Support

2.2.1 Structure of Rubidium

Rubidium has two isotopes, 85 and 87. The first has 72% abundance and the latter has 28% abundance [66]. We choose to use ^{87}Rb because of its wider frequency spacing between its hyperfine splitting lines compared to ^{85}Rb. As alkali atoms, rubidium contains a closed-cycle transition which is important for cooling. Rubidium has total electron momentum $\mathbf{J} = \mathbf{L} + \mathbf{S}$, where $\mathbf{L}$ is the orbital angular momentum and $\mathbf{S}$ is the spin angular momentum. In its ground state, $\mathbf{J} = 0 + \frac{1}{2} = \frac{1}{2}$ and in its first excited state $\mathbf{J} = 1 \pm \frac{1}{2} = \frac{1}{2}$ or $\frac{3}{2}$. The two different excited states have different energy levels, leading to two different transitions: D_1 transition ($5^2S_{1/2}$ to $5^2P_{1/2}$) and D_2 transition ($5^2S_{1/2}$ to $5^2P_{3/2}$). The total atomic angular momentum is given by $\mathbf{F} = \mathbf{J} + \mathbf{I}$, where $\mathbf{J}$ is the total electronic angular momentum and $\mathbf{I}$ is the nuclear spin ($I = \frac{3}{2}$ for ^{87}Rb). For the $5^2S_{1/2}$ ground state of ^{87}Rb, the allowed hyperfine levels are $F = 1$ and $F = 2$. In the D_2 excited state $5^2P_{3/2}$, the hyperfine levels are $F' = 0, 1, 2, 3$.

For electric dipole (E1) transitions, the hyperfine selection rules are $\Delta F = 0, \pm 1$ (but $F = 0 \not\leftrightarrow F' = 0$), as required by conservation of total angular momentum and the fact that the electric dipole operator is a rank-1 spherical tensor.

When an external magnetic field is applied, each hyperfine level F is split into $2F + 1$ Zeeman sublevels labeled by $m_F = -F, -F + 1, \ldots, F$. The energy shift of a Zeeman sublevel is given by

$$\Delta E = m_F \, g_F \, \mu_B \, B \tag{2.1}$$

where

$$g_F = g_J \frac{F(F+1) + J(J+1) - I(I+1)}{2F(F+1)} \tag{2.2}$$

and

$$g_J = g_L \frac{J(J+1) - S(S+1) + L(L+1)}{2J(J+1)} + g_S \frac{J(J+1) + S(S+1) - L(L+1)}{2J(J+1)}, \tag{2.3}$$

where $g_L = 1$ is the orbital g-factor and $g_S \approx 2.0023$ is the spin g-factor.

The Zeeman sublevel selection rules are $\Delta m_F = 0, \pm 1$, determined by the angular momentum carried by the photon: +1 for σ^+ polarization, −1 for σ^- polarization, and 0 for π polarization.

Taken together, these ingredients define the full energy level structure of ^{87}Rb. Starting from the electronic fine structure, the $5^2S_{1/2}$ ground state and $5^2P_{1/2,3/2}$ excited states are split by the spin-orbit interaction into the D_1 and D_2 lines. Each fine-structure level is further split into hyperfine manifolds labeled by F due to the coupling between the electronic angular momentum $\mathbf{J}$ and the nuclear spin $\mathbf{I}$. Finally, in the presence of an external magnetic field, each hyperfine level F is resolved into $2F+1$ Zeeman sublevels with projections m_F. The spectrum of rubidium, therefore, consists of well-organized fine, hyperfine, and Zeeman splittings, enabling us to use these structures to do laser cooling and trapping.

2.2.2 Laser Cooling

Velocity-Dependent Force

The most basic cooling technique we use is Doppler cooling. It cools atoms without trapping them spatially. We use the D_2 transition for ^{87}Rb, where we excite from $5^2S_{1/2}, F=2$ to $5^2P_{3/2}, F'=3$ as our cycling transition. During cycling, possible transitions include: $F=2 \rightarrow F'=3$ and $F=2 \rightarrow F'=2$. The latter transition is possible even if the laser frequency is not at exact resonance frequency due to the natural line width ($\Gamma = 6.0666$ MHz [48]) and the Doppler shift. The portion of atoms that would be excited to $F'=2$ can be calculated by

$$\frac{P_{F'=2}}{P_{F'=2}+P_{F'=3}} \tag{2.4}$$

and

$$P_{F'=i} \propto S_{F\rightarrow F'=i} \cdot L\big(\delta + \Delta_{i3}\big), \tag{2.5}$$

$S_{F\rightarrow F'}$ is the relative line strength, $L(\Delta) = \frac{1}{1+\left(\frac{2\Delta}{\Gamma}\right)^2}$ is the Lorentzian line shape, δ is the detuning from the $F'=3$ transition, Γ is the natural linewidth, and Δ_{i3} is the frequency separation between the $F'=i$ and $F'=3$ transitions.

For atoms excited to $5^2P_{3/2}, F'=2$, a portion of the atoms will fall to $5^2S_{1/2}, F=1$ level, which is a dark state, due to spontaneous emission. The exact branching ratio for spontaneous emission from an excited hyperfine level F' to a lower hyperfine level F within the same electronic state is given by

$$P_{F'\to F} = \frac{(2F+1)(2J+1)\begin{Bmatrix} J & J' & 1 \\ F' & F & I \end{Bmatrix}^2}{\sum\limits_{\tilde{F}}(2\tilde{F}+1)(2J+1)\begin{Bmatrix} J & J' & 1 \\ F' & \tilde{F} & I \end{Bmatrix}^2} \tag{2.6}$$

where $\{\dots\}$ denotes the Wigner 6-j symbol.

For ^{87}Rb with $I = \frac{3}{2}$, the decay from $5^2P_{3/2}$, $F' = 2$ ($J' = \frac{3}{2}$) to $5^2S_{1/2}$ ($J = \frac{1}{2}$) yields

$$P_{F'=2\to F=1} \approx 0.5, \quad P_{F'=2\to F=2} \approx 0.5. \tag{2.7}$$

Thus, approximately half of the atoms excited to $F' = 2$ will decay to the dark $F = 1$ state, requiring a repump laser to return them to the cooling cycle.

We use about 10% laser power at 6.6 GHz higher than the cycling transition frequency to excite atoms from $5^2S_{1/2}, F = 1$ to $5^2P_{3/2}, F' = 2$ to repump atoms back to the cycling transition. In the cooling transition, we slightly red detune our laser from this main transition frequency by approximately Δ. For an atom moving with velocity v along the laser beam direction, the Doppler effect shifts the frequency by:

$$\nu_{Doppler} \approx \nu\left(1 - \frac{v}{c}\right), \tag{2.8}$$

Thus, due to the Doppler effect, atoms moving toward the laser beam perceive the light as being shifted to a higher frequency (blue-shifted) and therefore closer to resonance. This increases their probability of interacting with the near-resonant laser. Atoms absorb photons from a well-defined direction repeatedly, they then re-emit them spontaneously in random directions. Each absorption event adds a momentum kick of magnitude $\hbar k$ to the atom in the direction of the incoming photon. Therefore, if the laser beam is arranged to oppose the atomic motion, this produces a velocity-dependent damping force that tends to reduce the atom's kinetic energy. By contrast, the momentum changes associated with spontaneous emission average to zero over many cycles because the emitted photons are radiated in random directions. As a result, the directed cooling effect from absorption dominates over the random kicks from emission, and the atomic ensemble cools on average.

We also need to consider the effect of power broadening. As the intensity increases and s_0 in 2.9 becomes significant, the transition linewidth is broadened from its natural value γ to an effective width $\gamma_{\text{eff}} = \gamma\sqrt{1+s_0}$. This broadening makes the atom respond to a wider range of Doppler shifts, effectively increasing the velocity interval and thus enlarging the capture velocity. At the same time, however, a larger s_0 reduces the slope of the force near $v = 0$ leading to weaker velocity dependent cooling, and the higher scattering rate enhances the momentum diffusion caused by random photon recoils. This balance between increasing capture range, reducing low-velocity damping, and increasing recoil heating due to higher power sets an optimal intensity regime for Doppler cooling [67, 68].

From [69], it summarizes this velocity-dependent force generated by two counter-propagating lasers by:

$$\vec{F}_{\text{OM}} \simeq \frac{8\hbar k^2 \delta s_0 \vec{v}}{\gamma\left[1 + s_0 + \left(\frac{2\delta}{\gamma}\right)^2\right]^2} \equiv -\beta\vec{v}, \tag{2.9}$$

Doppler cooling is limited by a balance between a velocity-dependent cooling force and the force caused by the random timing and direction of photon-scattering events. The random photon-scattering events cause heating in the atoms. The equilibrium between these effects defines the **Doppler limit**, the lowest temperature achievable for a two-level atom using Doppler cooling alone. This limit is given by

$$T_D = \frac{\hbar\Gamma}{2k_B}, \tag{2.10}$$

where Γ is the natural linewidth of the transition, k_B is the Boltzmann constant, and $\hbar$ is the reduced Planck constant. For the ^{87}Rb D_2 transition with $\Gamma/2\pi \approx 6.0666$ MHz, the Doppler limit temperature is [48]

$$T_D \approx 145.57\ \mu\text{K}. \tag{2.11}$$

By arranging a pair of counter-propagating, red-detuned cooling beams along each axis, Doppler cooling can be applied to that same intended axis. This configuration creates a viscous damping force on the atoms without providing spatial confinement, an arrangement commonly known as **optical molasses**.

Position-Dependent Force

To trap atoms in a fixed location, we require a position-dependent restoring force in addition to the velocity-dependent damping provided by optical molasses. In a MOT, this restoring force is generated via the Zeeman effect, which produces a position-dependent energy shift between different magnetic sublevels.

At the center of the trap, where we want to confine the atoms, the magnetic field is zero. Moving away from the center along a given axis, the magnetic field increases approximately linearly: $B(z) \approx b'z$, where b' is the magnetic field gradient. This field causes a Zeeman shift of the hyperfine sublevels, given by Eq. 2.1.

Along the magnetic field gradient axis, two counter-propagating red-detuned laser beams with opposite circular polarizations are applied: one σ^+, one σ^-. By the electric dipole selection rule, the magnetic quantum number can only change by $\Delta m_F = \pm 1$. Due to the conservation of angular momentum, a σ^+ polarized photon can only drive transitions with $\Delta m_F = +1$, while a σ^- photon can only drive transitions with $\Delta m_F = -1$. Each photon absorption transfers momentum $\hbar k$ to the atom in the beam's propagation direction.

Assume the B field increases linearly from left to right in a 1D example. For an atom positioned to the right of the origin ($B > 0$), the Zeeman effect shifts $\Delta m_F = +1$ transitions to higher frequency and $\Delta m_F = -1$ transitions to lower frequency. Since both beams are red-detuned from the zero-field resonance, the σ^- beam from the right will be closer to resonance than the σ^+ beam from the left, leading to a higher scattering rate from the σ^- beam. Each scattering event from this beam transfers momentum toward the trap center. On the opposite side of the trap, the situation reverses, but the force remains directed toward the center. The time-averaged spontaneous emission is isotropic, so it doesn't cause a net momentum change over many cycles, which is similar to the velocity-dependent cooling mechanism. The position-dependent detuning for each beam can be expressed as

$$\Delta'_{\sigma^{\pm}}(z) = \Delta \mp \frac{\mu_B g_F m_F b' z}{\hbar}, \tag{2.12}$$

where $\Delta < 0$ is the red detuning in the lab frame. This mechanism creates a spring-like restoring force in addition to the velocity-dependent damping from Doppler cooling, so that

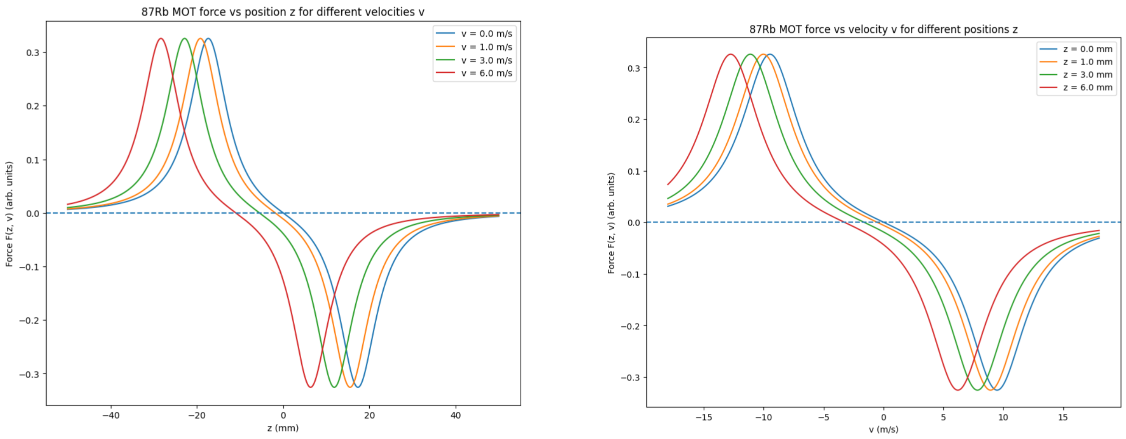

(a) MOT force as a function of position z for different atomic velocities.

(b) MOT force as a function of velocity v for different atomic positions.

Figure 2.1: Calculated magneto-optical trap force illustrating the position- and velocity-dependent restoring and damping components.

the total force along the gradient axis can be written approximately as

$$F(z,v) \approx -\alpha v - \kappa z, \tag{2.13}$$

where α is the damping coefficient, and κ is the MOT spring constant. In a 1D example, they can be written as:

$$\alpha(\delta) = 4\hbar k^2 \, \frac{I}{I_0} \, \frac{2\delta/\Gamma}{\left[1+(2\delta/\Gamma)^2\right]^2}, \tag{2.14}$$

$$\kappa(\delta) = \alpha(\delta) \, \frac{g_F \mu_B}{\hbar k} \, \frac{\partial B}{\partial z}. \tag{2.15}$$

Using arbitrary numbers, we can plot the two forces, as shown in Fig.2.13.

With the two forces combined, we can cool atoms by slowing them down in a damped harmonic oscillator, where Zeeman splitting causes the restoring force and Doppler cooling causes the damping force.

Chapter 3

EXPERIMENTAL SETUP

This chapter details the experimental setup and implementation for the 2D MOT portion of the quantum computer. It also covers some preparatory work for 2D+ and 3D MOT. The focus is on the architecture of the real-time control system, the design of the laser locking and distribution network, the generation and shaping of optical fields for cooling and trapping, and the mechanisms for imaging and manipulating the atomic cloud.

3.1 Control System design

Physical qubits are highly susceptible to environmental noise. Even subtle laser fluctuations can cause unintended errors. Precise quantum experiments demand a robust real-time control system capable of executing complex, time-sensitive sequences with nanosecond-level accuracy. We chose to use the Advanced Real-Time Infrastructure for Quantum physics (ARTIQ) as our real-time control framework. ARTIQ is an open-source control system developed through the joint efforts of NIST and various research groups. [70] It contains modular hardware and software components that support many different control signals required by our quantum system. A key advantage of ARTIQ is its ability to handle non-real-time operations—such as data acquisition, real-time analysis, predictions, and other computationally intensive tasks—concurrently with time-critical experiment execution. [71] This ensures the real-time physics sequence remains uninterrupted while background processing occurs. Additionally, ARTIQ offers a highly customizable user interface, enabling flexible experiment control and monitoring.

At the center of the ARTIQ box is the Xilinx FPGA, typically the Zynq-7000 or Artix-7 A100T series, depending on the version. The FPGA ensures deterministic latency because it avoids the scheduling uncertainty of a general-purpose operating system. It also provides nanosecond-level timing resolution while maintaining high flexibility to meet new demands.

This deterministic environment is crucial for the reproducibility of experiments and for implementing advanced protocols like quantum error correction.

3.1.1 Control Sequences

To use ARTIQ, we programmed dedicated control sequences. It opens all shutoff AOMs and shutters (if installed). And it may scan the double pass AOM frequency so that we can conduct characterization of the double pass AOM efficiency under different frequencies.

To conduct an actual experiment with high timing accuracy needs, we use this accurately timed 2D MOT Fluorescence Imaging sequence to detect the fluorescence of our cooled rubidium cloud. The most basic form of the control sequence is also simple: after heating the rubidium source, we turn on the MOT beams in both axes; wait 250 ms for the atoms to cool down and gather at the center; and then enable camera exposure for 150 µs to capture atom fluorescence due to cooling cycle transition. As shown in Fig. 3.2.

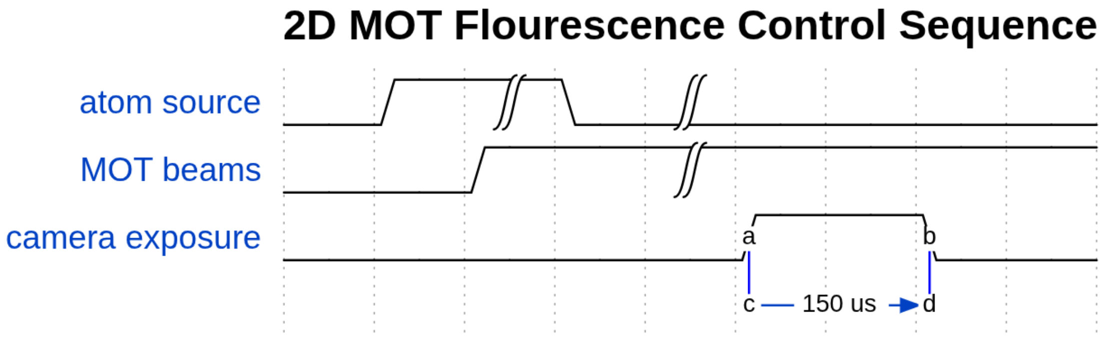

Figure 3.2: Basic control sequence for 2D MOT Fluorescence Imaging.

The atom source turn on time is not connected to the real-time control system, and we did not need to turn it on for every capture. After turning on the current supply to heat the atom dispenser source for about 10 minutes, the floating rubidium in the chamber is sufficient to sustain the experiment for several hours. Note: x axis not uniformly scaled.

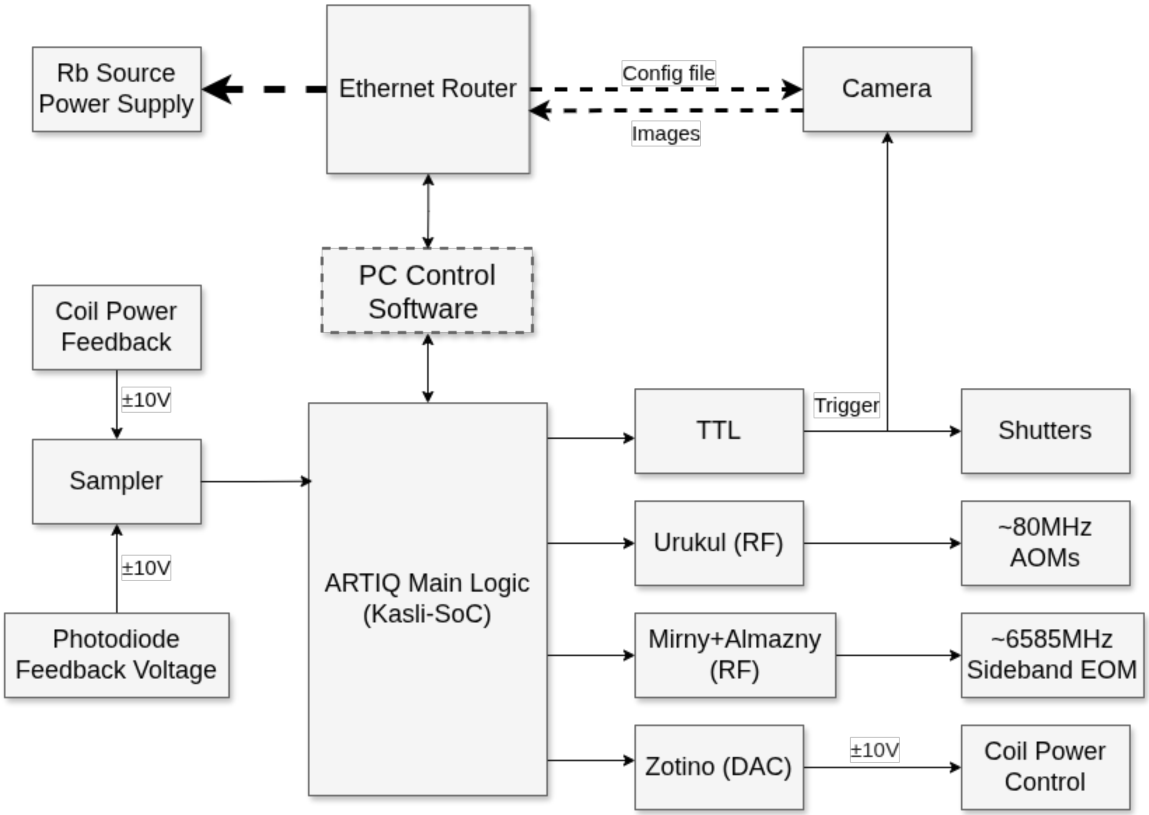

Figure 3.1: Block Diagram of Our Control System.

The overall system architecture integrates the ARTIQ control box, a main control PC, and auxiliary Ethernet-connected devices (e.g., scientific cameras, networked sensors) via a dedicated local lab network. This network handles high-bandwidth, non-time-critical data—such as fluorescence images from cameras—while all real-time signals are routed directly from the ARTIQ hardware to the experimental apparatus. As illustrated in this figure, the ARTIQ box provides a rich set of outputs, including digital TTL signals (for triggering cameras, shutters, or detectors), precisely tunable RF signals (for driving acousto-optic modulators and electro-optic modulators), and analog voltage outputs (for controlling magnetic fields, piezo actuators, or bias voltages). We also use ARTIQ to take real-time input and generate feedback loop. Eight-channel high precision ADC, Sampler, combined with Urukul, support PID feedback.

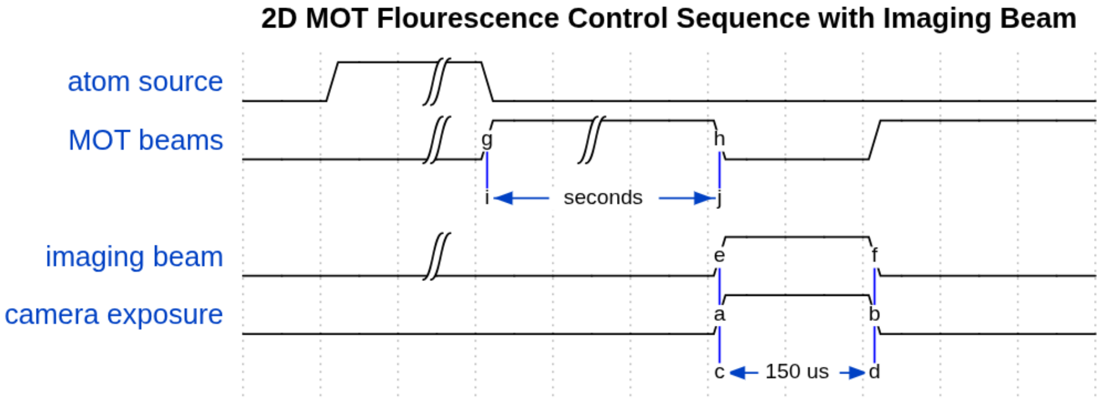

Figure 3.3: Control sequence for 2D MOT Fluorescence Imaging with imaging beam.

Similar to the previous experiment, atom source heating is only necessary a few times a day. We first turn on MOT beams to cool and trap atoms in the center region of the vacuum cell; then, turn off MOT beam, turn on imaging beam, and enable camera exposure at the exact same time.

To improve the Signal-to-Noise Ratio (SNR), we replace the MOT cooling beams with a dedicated imaging beam during exposure. This eliminates the scattered light and reflections from the MOT beams that otherwise contribute significant background noise in the camera images. The updated sequence is shown in Fig. 3.3. This separate imaging beam with isolated intensity, polarization, and detuning supports future optimization procedures, while reducing the disturbance to the MOT cooling system.

3.1.2 2D MOT Calibration Experiments

We first calibrated the system based on the delay of FLIR BFS-PGE-50S5M-C camera. The delay of the camera is verified using the following experiment (see Fig.3.4). After this calibration, we determined that the delay of the camera is approximately 50 µs. And this level of accuracy is enough for our current needs.

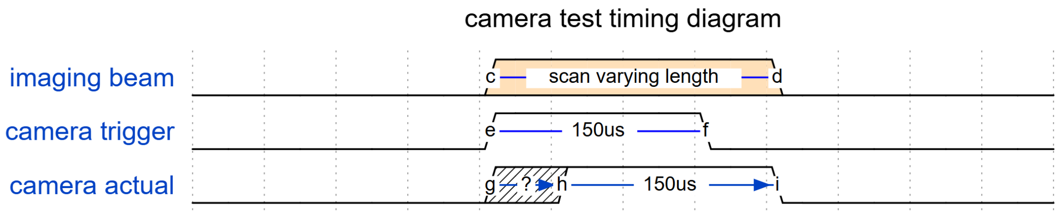

Figure 3.4: Control sequence for testing camera delay

In this calibration, we directly shine a laser beam to the camera CMOS. We fixed the camera exposure duration to 150 us, and repeat the experiment for varying imaging beam duration. We enable the imaging beam at the same time as camera trigger. Then, for scans with the imaging beam turn off earlier than the camera exposure actual stop, we would see a linear increase of fluorescence signal as imaging beam turn on time increase. Once the imaging beam turn off timestamp is after the after camera actual turn off, fluorescence signal would stay constant. Then we need to find the transition of fluorescence signal from linear increase to constant. The imaging beam turn on time length at that transition would be $delay + 150\mu s$.

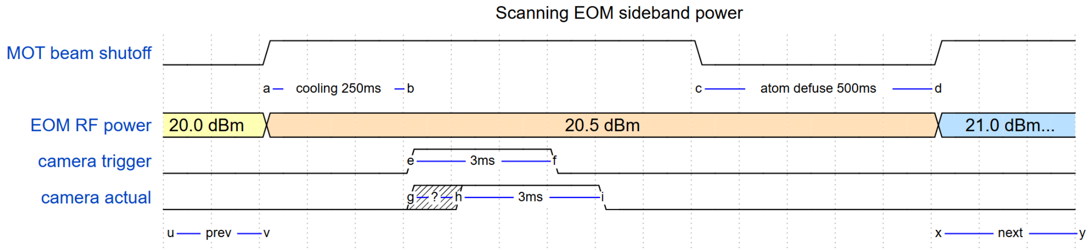

Figure 3.5: EOM power scan control sequence

In this experiment, we scan then power delivered to the sideband EOM from 17.5 dBm to 25.5 dBm, with 0.5 dB step size. For every EOM RF power data point, we conduct fluorescence experiment. Using MOT beams with corresponding sideband to cool atoms for 250 ms; then open camera shutter and expose for 3 ms; last, allow atom to defuse by turning off the MOT beams. An example result for this experiment is show in 4.3.

Then, we calibrated the EOM RF frequency/power and the cooling beam double-pass

AOM RF frequency using atomic cloud fluorescence. The experiments are shown below in Fig. 3.5, 4.3, 3.6, 4.2. In these experiments, we use MOT cooling beams only because we have carefully tuned our system to reduce scattered light and other noise. The atom source trigger is omitted in the following graphs since the atom density decays slowly, and turning the source on twice a day is sufficient for our purposes.

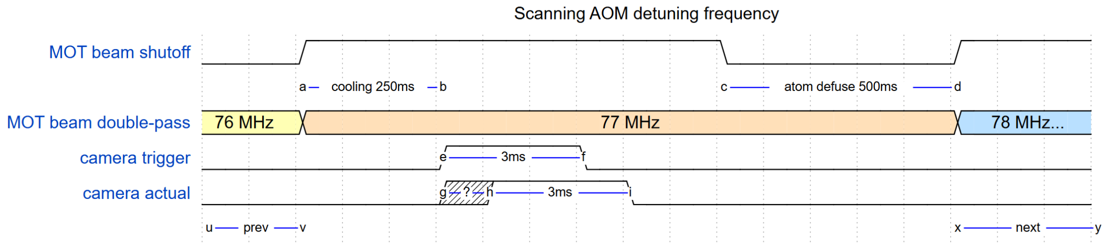

Figure 3.6: MOT Beam AOM Double-pass Frequency Scan Control Sequence

Similar to EOM power calibration experiment, this control sequence is intended to find the optimal MOT beam double-pass AOM frequency. For each data point, we first use MOT beam to cool atoms for 250 ms; then, trigger the camera 150 us exposure; finally turn off the MOT beams for 500 ms to allow all atoms defuse of the trap. An example result of this experiment is show in 4.2.

3.2 Saturated Absorption Spectroscopy

Saturated Absorption Spectroscopy (SAS) is an advanced method for locking the laser. Conducting simple spectroscopy is not enough to observe the hyperfine structures due to the Doppler broadening of the transition frequency. We want to eliminate the Doppler effect to obtain a clean and narrow spectroscopy line for each hyperfine transition. The Doppler broadening can be calculated by

$$\Delta\nu_D = \frac{2\nu_0}{c}\sqrt{\frac{2k_BT\ln 2}{m}} \tag{3.1}$$

where $\Delta\nu_D$ is the Doppler-broadened FWHM, ν_0 is the unshifted center frequency of the atomic transition, T is the absolute temperature of the atomic vapor, and m is the mass of the atom.

In our case, for ^{87}Rb at 300 K, $\Delta\nu_D = 511.3$ MHz. This is much larger than the natural linewidth of the ^{87}Rb D_2 transition: 6.06 MHz.

To remove Doppler broadening, we send two counter-propagating beams through a rubidium vapor cell: a weak probe and a stronger pump. Scanning the laser frequency and monitoring the probe transmission without the pump yields a broad, Doppler-broadened absorption profile because atoms with many longitudinal velocities satisfy the resonance condition. When the pump is added, it saturates the atoms whose longitudinal velocity is near zero (the same velocity class that the counter-propagating probe addresses at the same frequency). Saturation reduces the ground-to-excited population difference for that class, so those atoms absorb the probe less. As a result, a narrow Lamb dip (an increase in probe transmission) appears at each true hyperfine transition, superimposed on the Doppler pedestal. In multilevel spectra, additional crossover resonances often appear midway between nearby hyperfine lines, where atoms with nonzero velocities see the pump and probe resonant with different transitions.

3.3 RF Amplification System

3.3.1 Urukul Amplification

The Urukul (ARTIQ RF frequency synthesizer) is used to generate RF signals within the MHz range to control the AOMs. Generally, these AOMs require relatively high RF power. In our case, we used MT80-A1.5-IR from AA Opto-Electronic as our shutoff AOM and double pass AOM. It requires about 2 Watts of RF power, equivalent to 33 dBm. To amplify the Urukul output, we chose ZHL-5W-1X+ from Mini-Circuits. We set the DDS chip (AD9910) output amplitude to 1.0, the ARTIQ internal attenuator to 2.0 dB, and attached an external fix 25 dB attenuator (SA6HA-25 from Fairview Microwave). The ZHL-5W-1X+ provides 40 dB gain, boosting it to 33 dBm. External attenuators are used to prevent the system from software mistakes. Even with the minimum internal software-controlled attenuator, the final output power level would be under the maximum allowed RF power input for the AOM. To dissipate the heat from the amplifier, we mount the amplifiers directly on the water cooling plates (ATS-TCP-1003).

3.3.2 EOM RF Amplification

We use Mirny with the Almazny mezzanine to generate a 6.6 GHz RF signal. This signal is used to create a sideband for the 780 nm D2 laser to repump atoms back to the cooling transition from the dark state. We use an EOM, PM-Rb_6.6 from QUBIG, to generate this sideband. We provide 25 dBm to this EOM to generate about 10% of the sideband power. The output amplitude of Mirny is lower than expected, at only about -5 dBm. We used cascaded amplifiers due to the gain and output limitations of the amplifiers. We use ZVA-02203LN+ from Mini-Circuits as the first stage amplifier and ZVA-183WAX+ as the second stage amplifier. This configuration provides just enough RF power for the EOM to effectively generate the desired sideband.

Mode: Save | Recall
Type: PNG
Image Style: Normal | Inverted
Include Menu: Yes | No
Path Tips: Hold | Fade | None
Path Fade Time: 3.0s

C1 DC1M 1X 10.0mV/ FULL 29.3mV
C2 DC50 1X 1.00V/ FULL -3.02V
Timebase -76.0us 1.00ms/div 500kpts 50.0MSa/s
Trigger Auto Edge C2 DC 3.08V Rising

Figure 3.7: Fabry-Perot Interferometer measurement of the sideband EOM.

The repeating major peaks are the D2 transition frequency. The minor peaks are the first order 6.6 GHz sideband that exists on both side of the major peaks. The tiny peaks are the second order sideband that also exist on both side of the major peaks, where its distance are twice compare to the first order distance to the major peak.

3.4 Magnetic Field Setup

3.4.1 2D MOT Magnet

In the 2D MOT configuration, we used two orthogonal pairs of permanent magnets instead of conventional electromagnetic coils. These four magnets are precisely arranged, as illustrated in Fig.3.8, to generate a quadrupole magnetic field suitable for atom trapping. To maintain clear optical access for the cooling laser beams and to ensure that the magnetic field direction is aligned with the laser axis, we positioned the magnets at the diagonal corners of the glass cell. This geometry ensures that the beams can enter the glass cell perpendicularly, minimizing aberrations and maximizing beam overlap at the trap center.

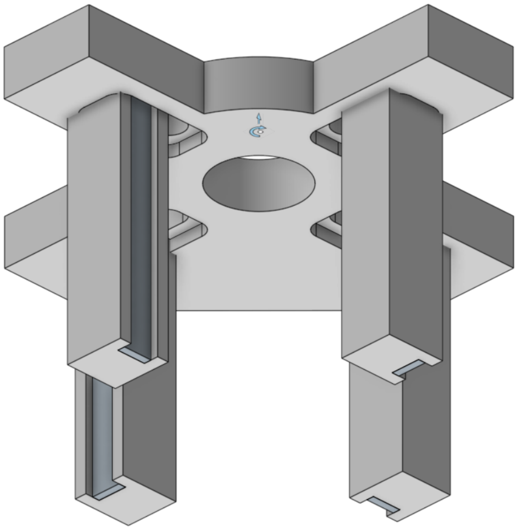

Figure 3.8: Configuration of 2D MOT magnets (rectangular cuboids) and their mount.

Each magnet is mounted on custom made aluminum magnet holder, which mounted on a two-axis translation stage, enabling fine adjustments of the magnetic field center relative to the glass cell. This flexibility is crucial for optimizing the overlap between the zero magnetic field and the optical molasses region. It also helps to position the atomic beam that will enter the 3D MOT through the small aperture in the differential pumping tube. We used the Python package `magpylib` to simulate the magnetic field distribution. According to the simulation, the magnetic field gradient at the trap center is approximately 18 G/cm. The field strength can be manually tuned by adjusting the distance between the magnets and the center of the glass cell, providing a simple yet effective means of field control. The Fluxgate Magnetometer FLUXMASTER confirmed that the actual field gradient in the central region can reach at least 20 G/cm; however, but due to limited time, we could not determine the final actual field gradient used in the setup.

3.4.2 3D MOT Anti-Helmholtz Coil Pair

We will use a pair of round electromagnetic coils to generate a quadrupole magnetic field. In the anti-Helmholtz setup, the coils carry equal currents in opposite directions, producing a magnetic field with a zero point at the center and a linear gradient along the axial direction. This configuration ensures a smooth and symmetric trapping potential for neutral atoms. Each coil is attached to a custom made water cooling plate, which prevents overheating and ensures consistent magnetic field performance.

In the coming month, we will use the TDK Lambda G20-50-U as the current source, with analog control support. The current transducer Danisense DS50UB-10V will be used to measure error signals and send feedback to the current source. This feedback will provide stabilized power to the 3D coil pair. Although some technical details have not been finalized yet, we are confident about this plan.

3.4.3 H Bridge for Anti-Helmholtz Coil

In the 3D MOT setup, H-bridge can switch the magnetic coil setup between anti-Helmholtz and Helmholtz. This enables us to explore more possibilities hidden in the atomic sublevels and different magnetic resonance. [72] For this purpose, we aim to design a high-current, low-noise H-bridge PCB for switching the current direction in the anti-Helmholtz coil. We are planning to implement the H-bridge with two Infineon IFX007T half-bridges.

3.5 MOT Optics

3.5.1 Laser Locking

Stable laser frequency and narrow linewidth are crucial for atomic cooling and precision spectroscopy experiments. For addressing rubidium D2 transitions at 780 nm, we use an external cavity diode laser (ECDL, TOPTICA) amplified by a tapered amplifier (TA), achieving approximately 4 W of total output power. A fraction of this power (approximately 50 mW) is directed toward modulation transfer spectroscopy (MTS) for laser locking.

The MTS setup utilizes a rubidium vapor reference cell. Here, an electro-optic modulator (EOM), driven by an arbitrary waveform generator (AWG), modulates a pump beam at 18 MHz. This modulated pump beam overlaps and counter-propagates with a probe beam inside the vapor cell. Nonlinear interactions (four-wave mixing) within the vapor medium transfer modulation from the pump beam to the probe beam. A lock-in amplifier demodulates this probe beam signal to generate a linear error signal, which is then fed into a proportional-integral-derivative (PID) controller (Moku:GO). The PID controller adjusts the ECDL frequency by finely controlling a piezo actuator that modifies the external cavity length. Following optimization, we were able to lock the laser at the resonance frequency with a standard deviation of $1.7 * 10^{-6}$ nm.

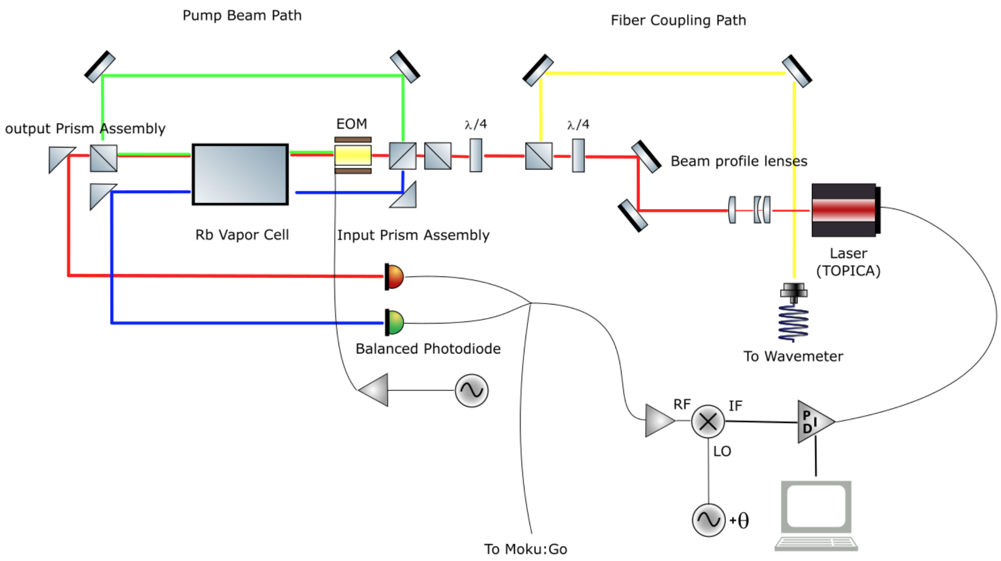

Figure 3.9: Laser Locking System Diagram.

The laser output is split into probe and pump paths and sent through a rubidium vapor cell for saturated absorption spectroscopy. An electro-optic modulator modulate the phase on the probe beam. The transmitted probe and reference signals are detected with a balanced photodiode, demodulated to generate an error signal, and fed back to the laser frequency actuator to stabilize the laser to an atomic transition.

3.5.2 Cooling Beam

The majority of the available 4 W laser power is allocated to the cooling beams. In our 2D MOT configuration, two cooling beams are used along the X and Y axes. For the Z-axis, a pushing beam and a retarding beam control the atom flux. Acousto-optic modulators (AOMs) play a critical role in beam distribution, providing rapid on-off control of the cooling beams.

Intensity control of the cooling beams is achieved through a combination of a half-wave plate (HWP) and a polarizing beam splitter cube (PBS), effectively forming a variable beam splitter. Each AOM utilized has a minimum diffraction efficiency of 85% in the first-order diffracted beam, as specified by the manufacturer [73].

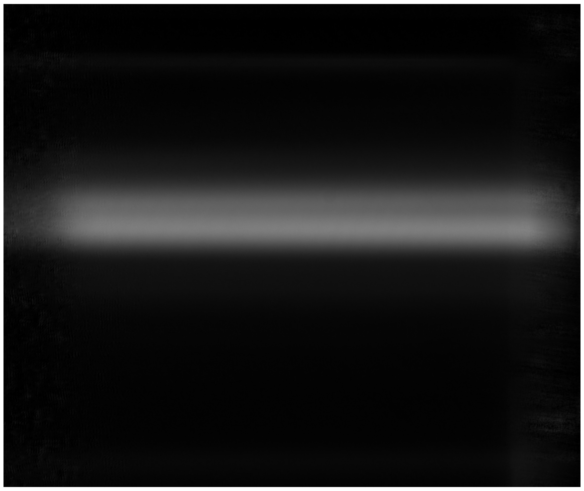

Figure 3.10: Fluorescence of Rubidium Vapor Cell

This is the fluorescence signal from the reference vapor cell. Upper beam is the probe beam and lower beam is the pump beam.

3.5.3 Repump Sideband

As mentioned in the Intro Section 2.2.2, we need repumping to bring atoms back to the cycling transition during the cooling process. We use a 6.6 GHz tunable EOM (Electro-optic modulator, QUBIG PM-Rb_6.6) to generate a 10% sideband with a 25 dBm RF power input. Then, we use the Thorlabs SA30-73 Fabry-Perot interferometer to check the sideband.

3.5.4 Double Pass AOM Frequency Shifter

A double-pass AOM configuration is employed to finely tune the laser frequency while maintaining stable coupling efficiency into optical fibers. As discussed previously, changing the input RF frequency to an AOM alters the diffraction angle according to the Bragg

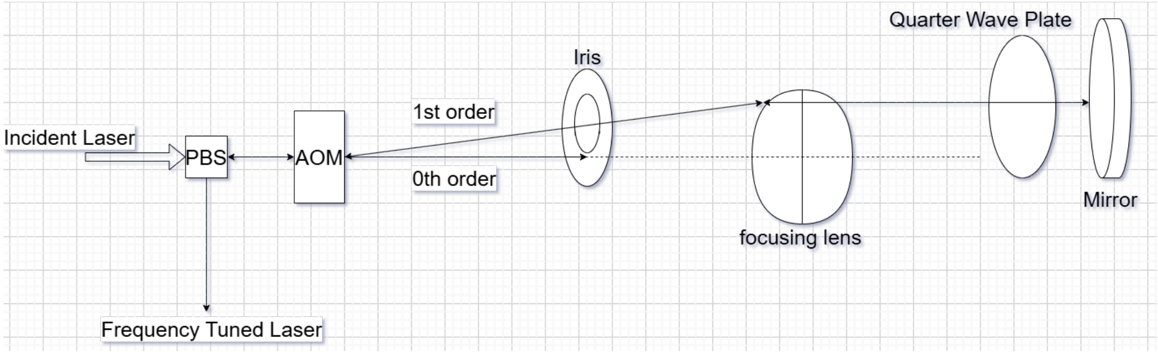

Figure 3.11: Double Pass AOM configuration

The incident laser is diffracted by an AOM. The first-order beam selected by an iris and retro reflected by a mirror through a quarter-wave plate twice to achieve a second pass through the AOM. This configuration doubles the frequency shift while canceling angular deviations.

diffraction condition:

$$n\lambda_{laser} = 2\Lambda_{acostic} \sin\theta$$

[74]. This feature is nice when we want to use the AOM as a switch to control the on/off state of a laser beam, but it is undesirable when we want to use the AOM to shift the laser frequency. During the in-coupling process, any slight change in laser direction could misalign the laser and cause us to lose laser power after the optical fiber.

For the frequency shifter, we want to use the AOM to tune the frequency while keeping the coupling efficiency stable. To compensate for the change in diffracted beam angle, we use a double pass setup in FIG.3.11. Due to physical limitations, the AOM has limited efficiency for different RF frequency inputs; thus, the double pass setup efficiency is also limited by that. Since the incident beam passes through the AOM twice, the final output beam will have twice the RF input frequency shift added to the incident beam.

3.5.5 Cooling Optics and Beam Expansion

Efficient atom cooling requires careful shaping of the cooling beams. To optimally cover the vacuum cell cross-section, beams exiting the optical fibers are expanded into elliptical shapes with a major axis of approximately 3.7 cm and a minor axis of approximately 1.2 cm.

Cylindrical lenses achieve this beam shaping. The resulting elliptical beam covers an area of approximately 3.48 cm^2. The saturation intensity (I_{sat}) for the rubidium-87 D2 transition is 1.669 mW/cm^2; thus, each cooling beam requires at least $1.669\text{mW/cm}^2 \times 3.48\text{cm}^2 \approx 5.8\text{mW}$ to reach saturation intensity.

Due to the absence of anti-reflection (AR) coatings on our vacuum cell glass surfaces, optical losses of roughly 4% per surface must be considered. Consequently, the counter-propagating beam experiences four additional surface reflections compared to the forward-propagating beam, resulting in approximately 85% transmission efficiency into the vacuum cell. Strategies for compensating for these optical losses include adjusting the input beam power and slightly defocusing the beam to maintain similar power intensity before and after the four additional reflections.

3.6 Imaging System

We need various ways to check the status of the system. Imaging the atoms is one of them. We use both fluorescence imaging and absorption imaging. With a similar shutoff AOM and double-pass AOM setup, we can also easily control the status of the imaging beam. We used TELEDYNE FLIR BFS-PGE-50S5M-C camera as our sensor. We shine the laser beam horizontally to the 45-degree slanted surface of the differential pumping tube; the reflected beam thus goes up through the vacuum cell then onto the camera sensor. Another camera is installed in a position such that the least amount of reflected laser light enters the camera, to observe the fluorescence of the atom cloud.

3.7 AOD Tweezers

Once we have the 3D MOT and SLM generated atom array, we need to use optical tweezers generated by two crossed AODs (Acousto-Optic Deflectors) to move the atoms. We chose the DSTX-400-830 from AA Opto Electronic. This AOD can achieve We have built a testing system for this setup, using an 830 nm diode laser and Thorlabs PDQ80A quadrant detector to measure the steering of the beam. Both AODs are installed on KM200PM kinetic mounts to ensure maximized efficiency. The first AOD is installed to steer horizontally, and the second is installed to steer vertically. Ideally, the second AOD should deflect the 1st order. Similar to the AOMs we use, these AODs also have varying diffraction efficiencies under different RF input frequencies, causing the

Chapter 4

RESULT

4.1 2D MOT Analysis

We observed clean 2D MOT signals, as shown in Fig.4.1. This was first trapped Rubidium 87 picture we got. However, in this picture, no background deduction was implemented. We have carefully tuned the optics so that minimum reflection light hits the CMOS camera.

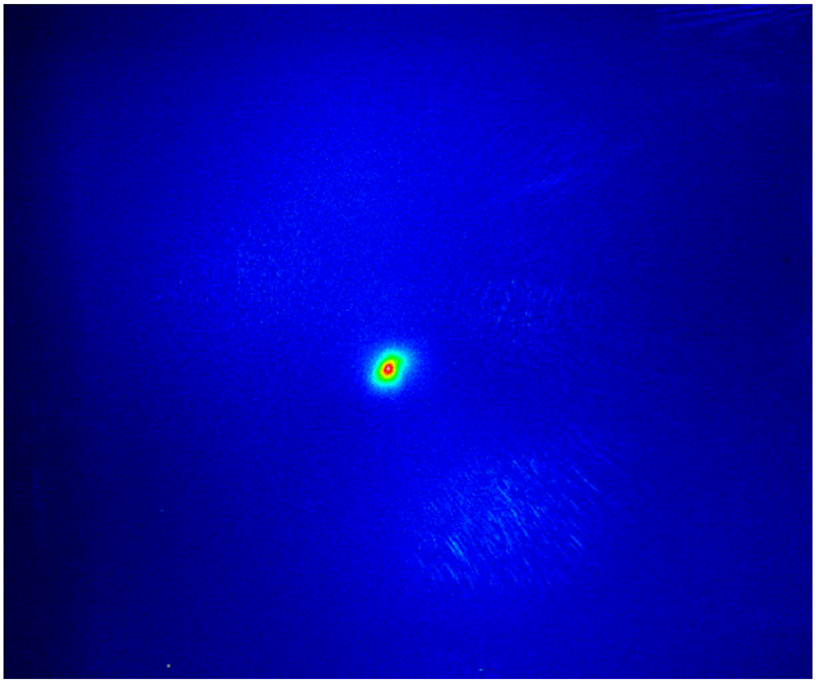

Figure 4.1: Heatmap image of Rubidium 87 atoms trapped in 2D MOT. The red means high intensity.

We used the control sequence in Fig.3.2 to measured the area averaged 2D MOT's fluorescence signal strength with different detuning frequency, as shown in Fig.4.2.

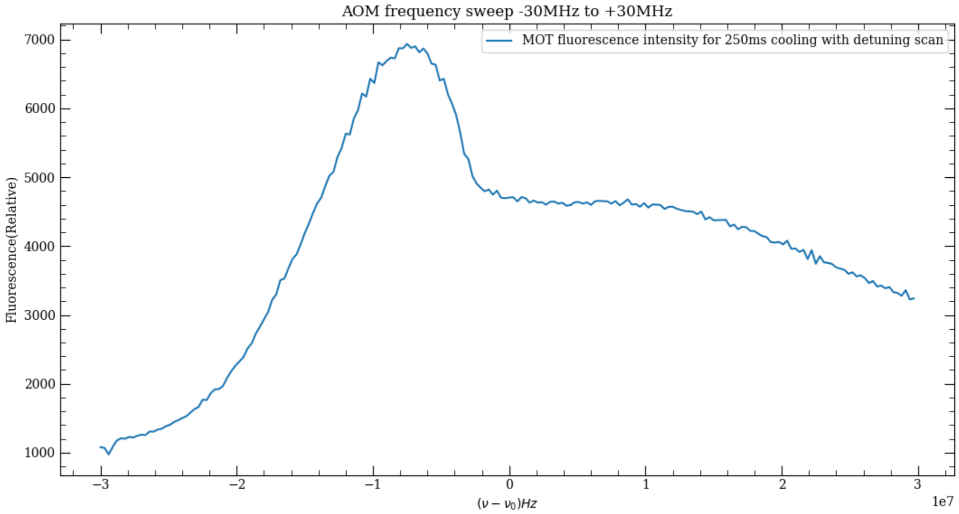

Figure 4.2: This plot is the averaged fluorescence signal strength at region of interest (MOT bright spot area) against the MOT cooling beam detuning frequency. Zero represents setting AOM to 80Mhz, which is exactly on resonance. And as expected, the intensity significantly decreases when we use detuning closer to zero compare to detuning at -8MHz, where the maximum fluorescence intensity is at.

In addition to tuning the cooling beam detuning using the AOM, we also investigated the dependence of the 2D MOT fluorescence on the EOM drive power. Varying the EOM RF power changes the distribution of optical power between the carrier and sideband frequencies, thereby modifying the effective cooling and repumping conditions. By scanning the RF power applied to the EOM, we measured the resulting change in the area-averaged MOT fluorescence, shown in Fig.4.3.

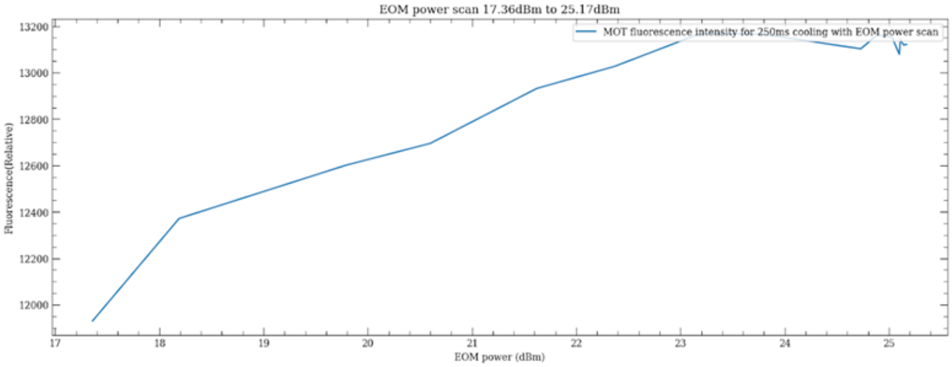

Figure 4.3: 2D MOT Fluorescence vs EOM Power

The y-axis is the fluorescence signal of 2D MOT. It reaches maximum when input RF power at about 23.5 dBm, but due to the limitation of current EOM RF amplifiers, we could not see the falling of fluorescence intensity as higher EOM RF power causing more laser power goes toward the 1st order laser sideband and reducing the 0th order carrier laser power.

We are still in the process of refining and calibrating the 2D MOT, but we have also collected some preliminary data for the 2D+ MOT atom beam.

4.2 2D+ MOT Atom Beam Analysis

We have successfully generated a 2D+ MOT atomic beam that sends cold atoms from the 2D MOT (source chamber) into the science chamber, as shown in Fig.4.4. This atomic beam will serve as the cold atom source for the loading of the 3D MOT.

Characterizing the atomic beam is essential for evaluating and optimizing the performance of the 2D+ MOT. Therefore, we performed transverse spectroscopy of the atomic beam. A probe beam was aligned in the x–y plane, perpendicular to the atomic beam propagation direction (z-axis). Frequency scans were performed at four different probe beam intensities, as shown in Fig.4.5, 4.6.

The measured spectra were fitted with Voigt profiles to extract the full width at half maximum (FWHM) at different probe beam saturation parameters. To estimate the Doppler

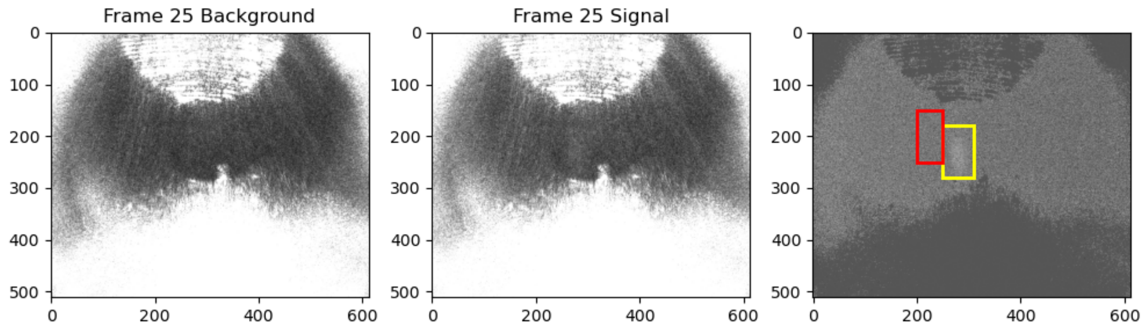

Figure 4.4: Background-subtracted fluorescence signal of the 2D+ MOT atomic beam under transverse probe illumination.

This signal is calculated by subtracting signal (MOT light on) from background (MOT light off) to generate the image on the far right. The signal is then the average pixel value in the yellow box minus the average pixel value in the red box, to normalize for camera value offsets and background light. This signal is then divided by a separate measurement of the fluorescence excitation power, to account for unwanted excitation intensity modulation from the AOM frequency shifter, at most 40% of the total drive power.

contribution to the linewidth, we used the empirical approximation

$$f_V \approx 0.5346 f_L + \sqrt{0.2166 f_L^2 + f_G^2}, \tag{4.1}$$

where f_L and f_G are the Lorentzian and Gaussian contributions to the linewidth, respectively.

As expected, the Lorentzian component of the Voigt profile increases with probe beam power. This is consistent with power broadening of the optical transition. However, the Gaussian component, which is associated with the transverse velocity distribution of the atomic beam, shows no clear dependence on the probe power.

A small blue shift of the resonance frequency is observed at higher probe powers. This effect may be due to the radiation pressure from the probe beam, which can accelerate atoms and therefore change their velocity distribution along the probe direction.

We still need to make several improvements. First, we have not yet saturated our probe beam to get a clear spectroscopy signal. Second, the signal amplitude has substantial day-

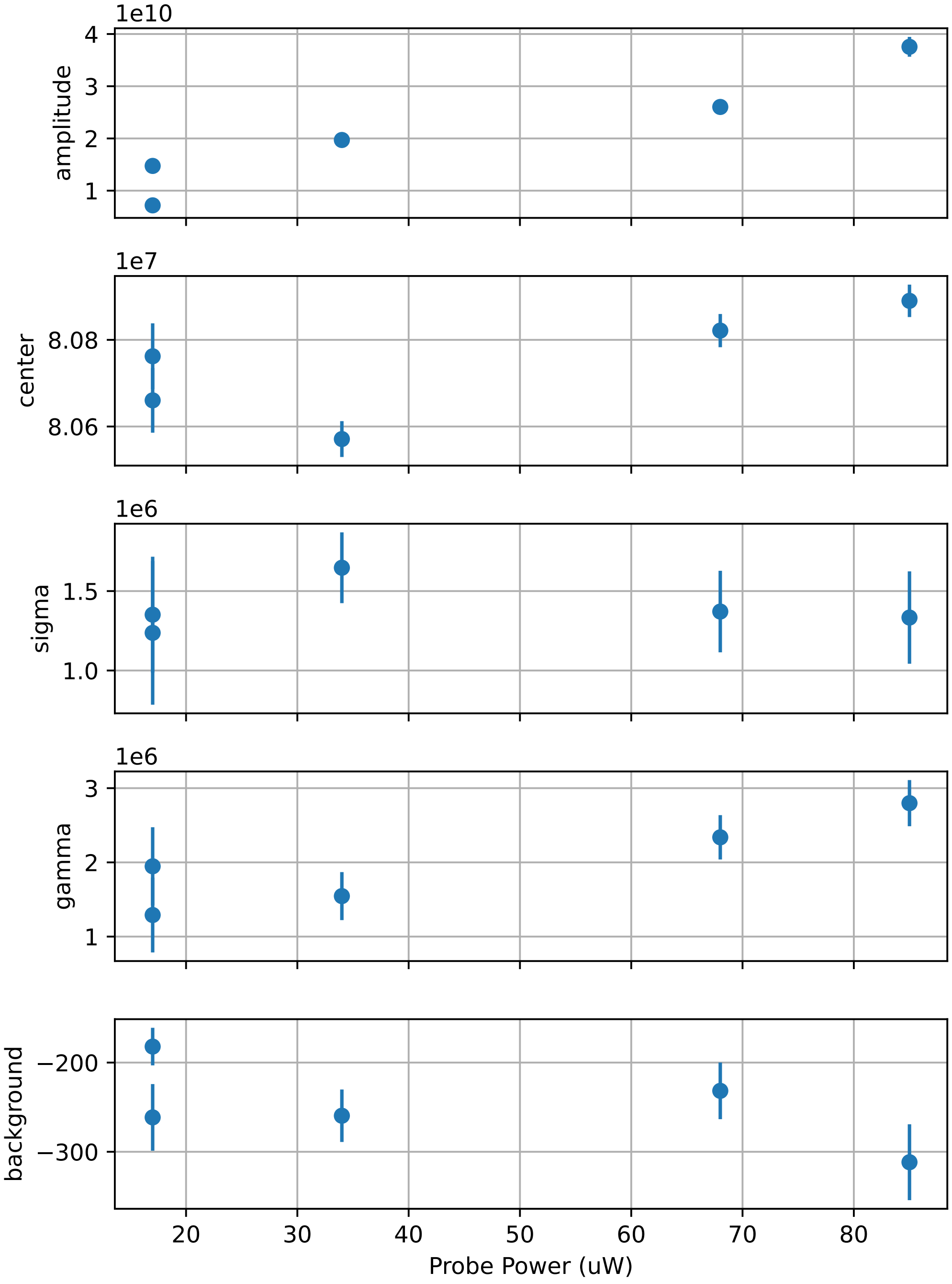

Figure 4.5: Extracted linewidth parameters as a function of probe beam power.

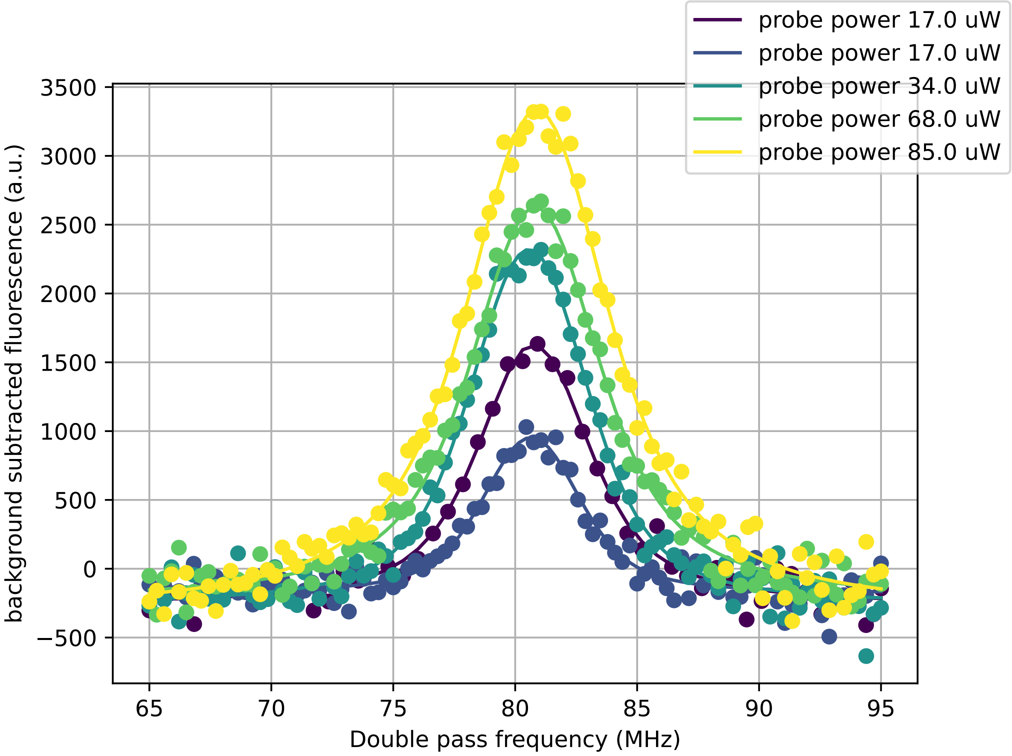

Figure 4.6: Representative spectroscopy data with Voigt profile fits.

to-day variation. This sensitivity may come from the relatively small probe beam waist and the fluctuations in the atomic beam trajectory caused by variations in the alignment of the 2D+ MOT push beam.

Chapter 5

FUTURE DIRECTIONS

In this section, I will outline a roadmap for the future development of the apparatus. The experiments so far have demonstrated a prototype 2D MOT of rubidium atoms and verified its would work as a cold-atom source. These results establish that the vacuum system, laser system, and control infrastructure function reliably enough to support the next stage of the project. Looking forward, the development plan separates into following three parts:

- Near-term Upgrades: This includes calibrating all electronics and optics parameters to optimize 2D MOT signal, building semi-automated control software to improve data collection efficiency, and rebuilding the vacuum system.

- Mid-term System Integration: This includes integrate the 3D MOT setup with the 2D+ MOT.

- Long-term Research Outlook: This includes single atom trapping, quantum many-body physics research, and advanced neutral atom quantum computer architecture like 3D atom array.

5.1 Near-Term Roadmap

Our current priority is to consistently generate a cold-atom beam into a the science chamber glass cell and to establish a 3D MOT there. The current 2D MOT will be converted into a 2D+ MOT by implementing the vertical push beam and a counter-propagating retarding beam. This configuration will create a directed atomic beam through the differential pumping aperture while preserving transverse cooling from the existing MOT beams. Once optimized, the 2D+ MOT will serve as an effective source for loading the 3D MOT and optical tweezers arrays.

Replacing the new science chamber glass cell is a central near-term task. A redesigned cell with improved smoother surface and AR coatings is expected to reduce reflections. This replacement will improve imaging fidelity and SLM atom array trap quality.

In parallel, several supporting subsystems will be upgraded. The vacuum system layout near the atom dispenser and source chamber ion pump will be modified to avoid a direct line of sight between the dispenser and the pump electrodes. This will improve long-term pump performance and increase the usable atomic flux into the 2D MOT trapping region. Active compensation coils around the science chamber will be installed and calibrated to cancel ambient magnetic fields, reducing Zeeman shifts and improving the stability of cooling and trapping conditions. These steps are standard for a modern neutral-atom platform, but they are essential to bring the apparatus to the point where it can reliably support larger-scale experiments.

5.2 Mid-Term Roadmap

In a few month, once we achieve the above targets on 2D+ MOT, the next step is to integrate with the 3D MOT, and trap individual atoms into programmable optical trap arrays generated by the SLM. The goal is to realize flexible 2D and 3D arrays of single atoms that can be rearranged and reconfigured in real time. Experiments in other groups have already shown that holographic methods, combined with atom rearrangement, can assemble 3D atom arrays that containing tens of atoms, with arbitrary geometry [75].

In our system, the SLM will be used to generate holographic phase patterns that create arrays of tightly focused micro-traps. We have already implemented and tested phase-retrieval algorithms such as Gerchberg–Saxton and Wirtinger Flow to compute the required SLM phase masks, and we have simulated 3D trap configurations based on these techniques. The generated image is shown in Fig.5.1. Numerical optimization and machine-learning-assisted algorithms will be used to improve trap uniformity and power efficiency, which are crucial for loading large arrays with only limited laser power.

To increase connectivity and explore error correction possibilities beyond planar arrangements, we plan to extend the trapping architecture into three dimensions by stacking multiple trap planes. 3D arrays offer two main advantages. First, they increase the number

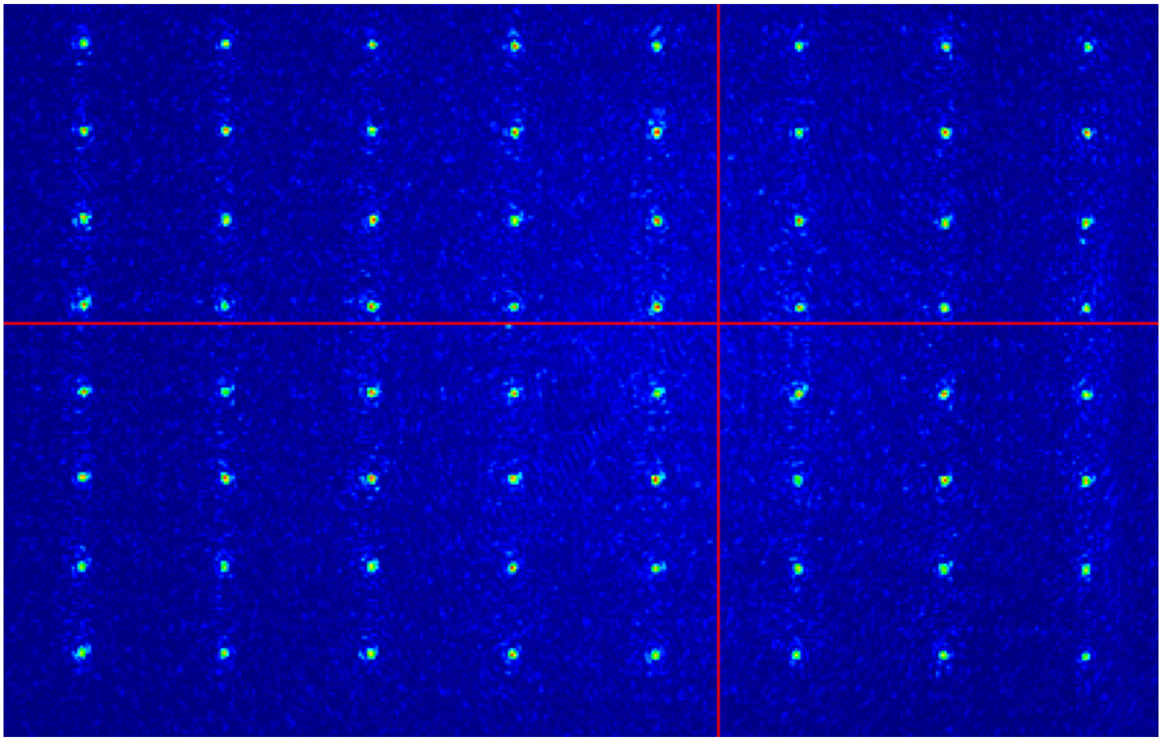

Figure 5.1: Camera captured 2D atoms array, generated by SLM using Gerchberg–Saxton algorithm. (From Kevin Wu)

of qubits that can be addressed within a given field of view and depth of focus. Second, they have better connectivity than a single 2D layer, which is helpful for arranging qubits in layouts that are better matched to quantum error-correcting codes.

Finally, acousto-optic deflectors (AODs) will be installed to realize reconfigurable optical tweezers that can move individual atoms within the array. It will fill vacancies to create defect-free patterns arrays, also move trapped atoms around to achieve all-to-all connectivity. Both usage are critical for creating neutral atom quantum computers.

5.3 Long-Term Roadmap

With large, controllable arrays in place, the next major goal is to realize high-fidelity entangling gates based on Rydberg interactions. This involves optimizing the control software and hardware. Recent work has shown that optimal-control techniques can design Ryd-

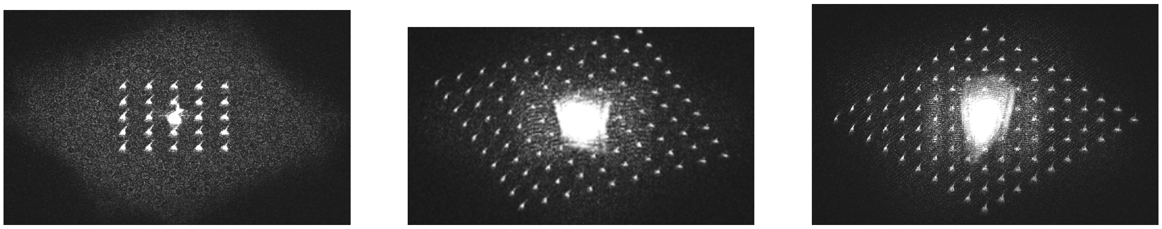

(a) Layer 1 (b) Layer 2 (c) Layer 3

Figure 5.2: SLM generated three layers of the 3D holographic atoms array. Captured using camera at different focus. (From Kevin Wu)

berg gates that achieve high theoretical fidelities while remaining compatible with realistic experimental parameters [76]. Building on these ideas, we also plan to explore optimized pulse sequences for multi-qubit Rydberg gates. We will develop calibration routines that characterize and compensate for pulse distortions, timing jitter, and amplitude drifts. These procedures will be automated where possible, so that gate parameters can be re-optimized in response to slow drifts in laser power, frequency, or beam alignment.

Beyond optimizing to achieve high fidelity, another motivation we have is to explore quantum error correction in different architectures. Recent experiments with Rydberg atom arrays have demonstrated logical qubits, repeated syndrome extraction, and loss-tolerant logical operations using surface and color codes on large, reconfigurable processors [41, 77]. In parallel, quantum LDPC codes have been developed that offer higher rates and lower overhead when the hardware can support long-range or three-dimensional connectivity [78].

Our 3D atom array architecture is designed to explore different types of codes. In the near term, we will test our setup with surface-code or color-code mapped onto 2D layers. At a later stage, 3D arrays and long-range Rydberg interactions can be used to implement small LDPC codes that benefit from the ability to connect distant qubits directly, reducing the number of swap operations or intermediate routing steps.

The motivation for building a three-dimensional neutral atom quantum processor is to go beyond proof-of-principle demonstrations and into a regime where reliable fault-tolerant logical qubits can execute algorithms that are genuinely hard for classical computers. A 3D atom array would scale cubically rather than quadratically compare to the classical 2D atom array. Combining the scale with low gate errors rates, the work in this thesis represents the first step toward that goal. We have laid the groundwork for a processor that can scale in both qubit number and code complexity. As the experiment evolves from small 2D code patches to fully 3D, long-range-connected arrays, it will provide a testbed for exploring which combinations of geometry, connectivity, and control lead most directly to practical quantum advantage. In this sense, the system developed here is not only a platform for neutral-atom quantum computing, but also a laboratory for discovering what a useful, fault-tolerant quantum computer should look like in practice.

BIBLIOGRAPHY

[1] Stephen P. Jordan. Quantum Algorithm Zoo.

[2] Lov K. Grover. A fast quantum mechanical algorithm for database search. In *Proceedings of the twenty-eighth annual ACM symposium on Theory of computing - STOC '96*, pages 212–219, Philadelphia, Pennsylvania, United States, 1996. ACM Press.

[3] Grover's algorithm description.

[4] Edward Farhi, Jeffrey Goldstone, and Sam Gutmann. A Quantum Approximate Optimization Algorithm, November 2014. arXiv:1411.4028.

[5] Guoming Wang. Efficient quantum algorithms for analyzing large sparse electrical networks. *Quantum Info. Comput.*, 17(11-12):987–1026, September 2017.

[6] John Preskill. Quantum Computing in the NISQ era and beyond. *Quantum*, 2:79, August 2018.

[7] R. Barends, J. Kelly, A. Megrant, A. Veitia, D. Sank, E. Jeffrey, T. C. White, J. Mutus, A. G. Fowler, B. Campbell, Y. Chen, Z. Chen, B. Chiaro, A. Dunsworth, C. Neill, P. O'Malley, P. Roushan, A. Vainsencher, J. Wenner, A. N. Korotkov, A. N. Cleland, and John M. Martinis. Superconducting quantum circuits at the surface code threshold for fault tolerance. *Nature*, 508(7497):500–503, April 2014.

[8] Aaron Somoroff, Quentin Ficheux, Raymond A. Mencia, Haonan Xiong, Roman Kuzmin, and Vladimir E. Manucharyan. Millisecond Coherence in a Superconducting Qubit. *Physical Review Letters*, 130(26):267001, June 2023.

[9] Yao-Yao Jiang, Chunqing Deng, Heng Fan, Bing-Yang Li, Luyan Sun, Xin-Sheng Tan, Weiting Wang, Guang-Ming Xue, Fei Yan, Hai-Feng Yu, Ying-Shan Zhang, Yu-Ran Zhang, and Chang-Ling Zou. Advancements in superconducting quantum computing. *National Science Review*, 12(8):nwaf246, June 2025.

[10] Frank Arute, Kunal Arya, Ryan Babbush, Dave Bacon, Joseph C. Bardin, Rami Barends, Rupak Biswas, Sergio Boixo, Fernando G. S. L. Brandao, David A. Buell, Brian Burkett, Yu Chen, Zijun Chen, Ben Chiaro, Roberto Collins, William Courtney, Andrew Dunsworth, Edward Farhi, Brooks Foxen, Austin Fowler, Craig Gidney, Marissa Giustina, Rob Graff, Keith Guerin, Steve Habegger, Matthew P. Harrigan, Michael J. Hartmann, Alan Ho, Markus Hoffmann, Trent Huang, Travis S. Humble,

Sergei V. Isakov, Evan Jeffrey, Zhang Jiang, Dvir Kafri, Kostyantyn Kechedzhi, Julian Kelly, Paul V. Klimov, Sergey Knysh, Alexander Korotkov, Fedor Kostritsa, David Landhuis, Mike Lindmark, Erik Lucero, Dmitry Lyakh, Salvatore Mandrà, Jarrod R. McClean, Matthew McEwen, Anthony Megrant, Xiao Mi, Kristel Michielsen, Masoud Mohseni, Josh Mutus, Ofer Naaman, Matthew Neeley, Charles Neill, Murphy Yuezhen Niu, Eric Ostby, Andre Petukhov, John C. Platt, Chris Quintana, Eleanor G. Rieffel, Pedram Roushan, Nicholas C. Rubin, Daniel Sank, Kevin J. Satzinger, Vadim Smelyanskiy, Kevin J. Sung, Matthew D. Trevithick, Amit Vainsencher, Benjamin Villalonga, Theodore White, Z. Jamie Yao, Ping Yeh, Adam Zalcman, Hartmut Neven, and John M. Martinis. Quantum supremacy using a programmable superconducting processor. *Nature*, 574(7779):505–510, October 2019.

[11] Thomas Strohm, Karen Wintersperger, Florian Dommert, Daniel Basilewitsch, Georg Reuber, Andrey Hoursanov, Thomas Ehmer, Davide Vodola, and Sebastian Luber. Ion-Based Quantum Computing Hardware: Performance and End-User Perspective, May 2024. arXiv:2405.11450 [quant-ph].

[12] Quantinuum System Model H2 Product Data Sheet, August 2023.

[13] D. Kielpinski, C. Monroe, and D. J. Wineland. Architecture for a large-scale ion-trap quantum computer. *Nature*, 417(6890):709–711, June 2002.

[14] C. Monroe, R. Raussendorf, A. Ruthven, K. R. Brown, P. Maunz, L.-M. Duan, and J. Kim. Large-scale modular quantum-computer architecture with atomic memory and photonic interconnects. *Physical Review A*, 89(2):022317, February 2014.

[15] Dominic Widdows and Amit Bhattacharyya. Quantum Financial Modeling on Noisy Intermediate-Scale Quantum Hardware: Random Walks Using Approximate Quantum Counting. *Quantum Economics and Finance*, 1(1):5–20, June 2024.

[16] Sang Hyub Kim, Jonathan Mei, Claudio Girotto, Masako Yamada, and Martin Roetteler. Quantum Large Language Model Fine-Tuning, April 2025. arXiv:2504.08732 [quant-ph].

[17] H. J. Kimble. The quantum internet. *Nature*, 453(7198):1023–1030, June 2008. Publisher: Nature Publishing Group.

[18] Sergei Slussarenko and Geoff J. Pryde. Photonic quantum information processing: A concise review. *Applied Physics Reviews*, 6(4):041303, October 2019.

[19] Dennis Delali Kwesi Wayo, Leonardo Goliatt, and Darvish Ganji. Linear Optics to Scalable Photonic Quantum Computing, January 2025. arXiv:2501.02513 [quant-ph].

[20] Emanuele Pelucchi, Giorgos Fagas, Igor Aharonovich, Dirk Englund, Eden Figueroa, Qihuang Gong, Hübel Hannes, Jin Liu, Chao-Yang Lu, Nobuyuki Matsuda, Jian-Wei Pan, Florian Schreck, Fabio Sciarrino, Christine Silberhorn, Jianwei Wang, and Klaus D. Jöns. The potential and global outlook of integrated photonics for quantum technologies. *Nature Reviews Physics*, 4(3):194–208, March 2022.

[21] Jacquiline Romero and Gerard Milburn. Photonic Quantum Computing, April 2024. arXiv:2404.03367 [quant-ph].

[22] H. Aghaee Rad, T. Ainsworth, R. N. Alexander, B. Altieri, M. F. Askarani, R. Baby, L. Banchi, B. Q. Baragiola, J. E. Bourassa, R. S. Chadwick, I. Charania, H. Chen, M. J. Collins, P. Contu, N. D'Arcy, G. Dauphinais, R. De Prins, D. Deschenes, I. Di Luch, S. Duque, P. Edke, S. E. Fayer, S. Ferracin, H. Ferretti, J. Gefaell, S. Glancy, C. González-Arciniegas, T. Grainge, Z. Han, J. Hastrup, L. G. Helt, T. Hillmann, J. Hundal, S. Izumi, T. Jaeken, M. Jonas, S. Kocsis, I. Krasnokutska, M. V. Larsen, P. Laskowski, F. Laudenbach, J. Lavoie, M. Li, E. Lomonte, C. E. Lopetegui, B. Luey, A. P. Lund, C. Ma, L. S. Madsen, D. H. Mahler, L. Mantilla Calderón, M. Menotti, F. M. Miatto, B. Morrison, P. J. Nadkarni, T. Nakamura, L. Neuhaus, Z. Niu, R. Noro, K. Papirov, A. Pesah, D. S. Phillips, W. N. Plick, T. Rogalsky, F. Rortais, J. Sabines-Chesterking, S. Safavi-Bayat, E. Sazhaev, M. Seymour, K. Rezaei Shad, M. Silverman, S. A. Srinivasan, M. Stephan, Q. Y. Tang, J. F. Tasker, Y. S. Teo, R. B. Then, J. E. Tremblay, I. Tzitrin, V. D. Vaidya, M. Vasmer, Z. Vernon, L. F. S. S. M. Villalobos, B. W. Walshe, R. Weil, X. Xin, X. Yan, Y. Yao, M. Zamani Abnili, and Y. Zhang. Scaling and networking a modular photonic quantum computer. *Nature*, 638(8052):912–919, February 2025.

[23] Daniel Litinski and Naomi Nickerson. Active volume: An architecture for efficient fault-tolerant quantum computers with limited non-local connections, November 2022. arXiv:2211.15465 [quant-ph].

[24] Guido Burkard, Thaddeus D. Ladd, Andrew Pan, John M. Nichol, and Jason R. Petta. Semiconductor spin qubits. *Reviews of Modern Physics*, 95(2):025003, June 2023.

[25] A. M. J. Zwerver, T. Krähenmann, T. F. Watson, L. Lampert, H. C. George, R. Pillarisetty, S. A. Bojarski, P. Amin, S. V. Amitonov, J. M. Boter, R. Caudillo, D. Correas-Serrano, J. P. Dehollain, G. Droulers, E. M. Henry, R. Kotlyar, M. Lodari, F. Lüthi, D. J. Michalak, B. K. Mueller, S. Neyens, J. Roberts, N. Samkharadze, G. Zheng, O. K. Zietz, G. Scappucci, M. Veldhorst, L. M. K. Vandersypen, and J. S. Clarke. Qubits made by advanced semiconductor manufacturing. *Nature Electronics*, 5(3):184–190, March 2022.

[26] Yi-Hsien Wu, Leon C. Camenzind, Patrick Bütler, Ik Kyeong Jin, Akito Noiri, Kenta Takeda, Takashi Nakajima, Takashi Kobayashi, Giordano Scappucci, Hsi-Sheng Goan, and Seigo Tarucha. Simultaneous High-Fidelity Single-Qubit Gates in a Spin Qubit Array, July 2025. arXiv:2507.11918 [quant-ph].

[27] Jonathan Y. Huang, Rocky Y. Su, Wee Han Lim, MengKe Feng, Barnaby van Straaten, Brandon Severin, Will Gilbert, Nard Dumoulin Stuyck, Tuomo Tanttu, Santiago Serrano, Jesus D. Cifuentes, Ingvild Hansen, Amanda E. Seedhouse, Ensar Vahapoglu, Ross C. C. Leon, Nikolay V. Abrosimov, Hans-Joachim Pohl, Michael L. W. Thewalt, Fay E. Hudson, Christopher C. Escott, Natalia Ares, Stephen D. Bartlett, Andrea Morello, Andre Saraiva, Arne Laucht, Andrew S. Dzurak, and Chih Hwan Yang. High-fidelity spin qubit operation and algorithmic initialization above 1 K. *Nature*, 627(8005):772–777, March 2024.

[28] Hannah J. Manetsch, Gyohei Nomura, Elie Bataille, Kon H. Leung, Xudong Lv, and Manuel Endres. A tweezer array with 6100 highly coherent atomic qubits, July 2025. arXiv:2403.12021 [quant-ph].

[29] Karen Wintersperger, Florian Dommert, Thomas Ehmer, Andrey Hoursanov, Johannes Klepsch, Wolfgang Mauerer, Georg Reuber, Thomas Strohm, Ming Yin, and Sebastian Luber. Neutral atom quantum computing hardware: performance and end-user perspective. *EPJ Quantum Technology*, 10(1):1–26, December 2023.

[30] Ben W. Reichardt, Adam Paetznick, David Aasen, Ivan Basov, Juan M. Bello-Rivas, Parsa Bonderson, Rui Chao, Wim van Dam, Matthew B. Hastings, Ryan V. Mishmash, Andres Paz, Marcus P. da Silva, Aarthi Sundaram, Krysta M. Svore, Alexander Vaschillo, Zhenghan Wang, Matt Zanner, William B. Cairncross, Cheng-An Chen, Daniel Crow, Hyosub Kim, Jonathan M. Kindem, Jonathan King, Michael McDonald, Matthew A. Norcia, Albert Ryou, Mark Stone, Laura Wadleigh, Katrina Barnes, Peter Battaglino, Thomas C. Bohdanowicz, Graham Booth, Andrew Brown, Mark O. Brown, Kayleigh Cassella, Robin Coxe, Jeffrey M. Epstein, Max Feldkamp, Christopher Griger, Eli Halperin, Andre Heinz, Frederic Hummel, Matthew Jaffe, Antonia M. W. Jones, Eliot Kapit, Krish Kotru, Joseph Lauigan, Ming Li, Jan Marjanovic, Eli Megidish, Matthew Meredith, Ryan Morshead, Juan A. Muniz, Sandeep Narayanaswami, Ciro Nishiguchi, Timothy Paule, Kelly A. Pawlak, Kristen L. Pudenz, David Rodríguez Pérez, Jon Simon, Aaron Smull, Daniel Stack, Miroslav Urbanek, René J. M. van de Veerdonk, Zachary Vendeiro, Robert T. Weverka, Thomas Wilkason, Tsung-Yao Wu, Xin Xie, Evan Zalys-Geller, Xiaogang Zhang, and Benjamin J. Bloom. Fault-tolerant quantum computation with a neutral atom processor, June 2025. arXiv:2411.11822.

[31] Jonathan Wurtz, Alexei Bylinskii, Boris Braverman, Jesse Amato-Grill, Sergio H. Cantu, Florian Huber, Alexander Lukin, Fangli Liu, Phillip Weinberg, John Long, Sheng-Tao Wang, Nathan Gemelke, and Alexander Keesling. Aquila: QuEra's 256-qubit neutral-atom quantum computer, June 2023. arXiv:2306.11727 [quant-ph].

[32] M. Saffman, T. G. Walker, and K. Mølmer. Quantum information with Rydberg atoms. *Reviews of Modern Physics*, 82(3):2313–2363, August 2010.

[33] D. Jaksch, J. I. Cirac, P. Zoller, S. L. Rolston, R. Côté, and M. D. Lukin. Fast Quantum Gates for Neutral Atoms. *Physical Review Letters*, 85(10):2208–2211, September 2000.

[34] Simon J. Evered, Dolev Bluvstein, Marcin Kalinowski, Sepehr Ebadi, Tom Manovitz, Hengyun Zhou, Sophie H. Li, Alexandra A. Geim, Tout T. Wang, Nishad Maskara, Harry Levine, Giulia Semeghini, Markus Greiner, Vladan Vuletić, and Mikhail D. Lukin. High-fidelity parallel entangling gates on a neutral-atom quantum computer. *Nature*, 622(7982):268–272, October 2023.

[35] Loïc Henriet, Lucas Beguin, Adrien Signoles, Thierry Lahaye, Antoine Browaeys, Georges-Olivier Reymond, and Christophe Jurczak. Quantum computing with neutral atoms. *Quantum*, 4:327, September 2020.

[36] Shuo Ma, Alex P. Burgers, Genyue Liu, Jack Wilson, Bichen Zhang, and Jeff D. Thompson. Universal Gate Operations on Nuclear Spin Qubits in an Optical Tweezer Array of $^{171}\mathrm{Yb}$ Atoms. *Physical Review X*, 12(2):021028, May 2022. Publisher: American Physical Society.

[37] Jessie T. Zhang, Lewis R. B. Picard, William B. Cairncross, Kenneth Wang, Yichao Yu, Fang Fang, and Kang-Kuen Ni. An optical tweezer array of ground-state polar molecules, December 2021. arXiv:2112.00991 [physics].

[38] L. Isenhower, E. Urban, X. L. Zhang, A. T. Gill, T. Henage, T. A. Johnson, T. G. Walker, and M. Saffman. Demonstration of a Neutral Atom Controlled-NOT Quantum Gate. *Physical Review Letters*, 104(1):010503, January 2010. Publisher: American Physical Society.

[39] Hannes Bernien, Sylvain Schwartz, Alexander Keesling, Harry Levine, Ahmed Omran, Hannes Pichler, Soonwon Choi, Alexander S. Zibrov, Manuel Endres, Markus Greiner, Vladan Vuletić, and Mikhail D. Lukin. Probing many-body dynamics on a 51-atom quantum simulator. *Nature*, 551(7682):579–584, November 2017. Publisher: Nature Publishing Group.

[40] Sepehr Ebadi, Tout T. Wang, Harry Levine, Alexander Keesling, Giulia Semeghini, Ahmed Omran, Dolev Bluvstein, Rhine Samajdar, Hannes Pichler, Wen Wei Ho, Soonwon Choi, Subir Sachdev, Markus Greiner, Vladan Vuletić, and Mikhail D. Lukin. Quantum phases of matter on a 256-atom programmable quantum simulator. *Nature*, 595(7866):227–232, July 2021. Publisher: Nature Publishing Group.

[41] Dolev Bluvstein, Simon J. Evered, Alexandra A. Geim, Sophie H. Li, Hengyun Zhou, Tom Manovitz, Sepehr Ebadi, Madelyn Cain, Marcin Kalinowski, Dominik Hangleiter, J. Pablo Bonilla Ataides, Nishad Maskara, Iris Cong, Xun Gao, Pedro Sales Rodriguez, Thomas Karolyshyn, Giulia Semeghini, Michael J. Gullans, Markus Greiner, Vladan Vuletić, and Mikhail D. Lukin. Logical quantum processor based on reconfigurable atom arrays. *Nature*, 626(7997):58–65, February 2024.

[42] Alec Jenkins, Joanna W. Lis, Aruku Senoo, William F. McGrew, and Adam M. Kaufman. Ytterbium Nuclear-Spin Qubits in an Optical Tweezer Array. *Physical Review X*, 12(2):021027, May 2022. Publisher: American Physical Society.

[43] Ivaylo S. Madjarov, Jacob P. Covey, Adam L. Shaw, Joonhee Choi, Anant Kale, Alexandre Cooper, Hannes Pichler, Vladimir Schkolnik, Jason R. Williams, and Manuel Endres. High-fidelity entanglement and detection of alkaline-earth Rydberg atoms. *Nature Physics*, 16(8):857–861, August 2020. Publisher: Nature Publishing Group.

[44] D. DeMille. Quantum Computation with Trapped Polar Molecules. *Physical Review Letters*, 88(6):067901, January 2002. Publisher: American Physical Society.

[45] Lewis R. B. Picard, Annie J. Park, Gabriel E. Patenotte, Samuel Gebretsadkan, David Wellnitz, Ana Maria Rey, and Kang-Kuen Ni. Sub-millisecond Entanglement and iSWAP Gate between Molecular Qubits. *Nature*, 637(8047):821–826, January 2025. arXiv:2406.15345 [physics].

[46] A. Trautmann, P. Ilzhöfer, G. Durastante, C. Politi, M. Sohmen, M.J. Mark, and F. Ferlaino. Dipolar Quantum Mixtures of Erbium and Dysprosium Atoms. *Physical Review Letters*, 121(21):213601, November 2018. Publisher: American Physical Society.

[47] D. P. Divincenzo. Topics in Quantum Computers. In Lydia L. Sohn, Leo P. Kouwenhoven, and Gerd Schön, editors, *Mesoscopic Electron Transport*, pages 657–677. Springer Netherlands, Dordrecht, 1997.

[48] Daniel Steck. Rubidium 87 D Line Data (revision 2.3.3). May 2024.

[49] T.M. Graham, L. Phuttitarn, R. Chinnarasu, Y. Song, C. Poole, K. Jooya, J. Scott, A. Scott, P. Eichler, and M. Saffman. Midcircuit Measurements on a Single-Species Neutral Alkali Atom Quantum Processor. *Physical Review X*, 13(4):041051, December 2023.

[50] Simon J Devitt, William J Munro, and Kae Nemoto. Quantum error correction for beginners. *Reports on Progress in Physics*, 76(7):076001, June 2013.

[51] Victor V. Albert and Philippe Faist. The Error Correction Zoo. 2025.

[52] Daniel Gottesman. Stabilizer Codes and Quantum Error Correction, May 1997. arXiv:quant-ph/9705052.

[53] A. M. Steane. Error Correcting Codes in Quantum Theory. *Physical Review Letters*, 77(5):793–797, July 1996.

[54] Peter W. Shor. Scheme for reducing decoherence in quantum computer memory. *Physical Review A*, 52(4):R2493–R2496, October 1995.

[55] A. Yu. Kitaev. Fault-tolerant quantum computation by anyons. *Annals of Physics*, 303(1):2–30, January 2003.

[56] Austin G. Fowler, Matteo Mariantoni, John M. Martinis, and Andrew N. Cleland. Surface codes: Towards practical large-scale quantum computation. *Physical Review A*, 86(3):032324, September 2012.

[57] H. Bombin and M. A. Martin-Delgado. Topological Quantum Distillation. *Physical Review Letters*, 97(18):180501, October 2006.

[58] P. T. Cochrane, G. J. Milburn, and W. J. Munro. Macroscopically distinct quantum-superposition states as a bosonic code for amplitude damping. *Physical Review A*, 59(4):2631–2634, April 1999.

[59] Debbie W. Leung, M. A. Nielsen, Isaac L. Chuang, and Yoshihisa Yamamoto. Approximate quantum error correction can lead to better codes. *Physical Review A*, 56(4):2567–2573, October 1997.

[60] The Nobel Prize in Physics 1997.

[61] Ingo Nosske, Luc Couturier, Fachao Hu, Canzhu Tan, Chang Qiao, Jan Blume, Y. H. Jiang, Peng Chen, and Matthias Weidemüller. Two-dimensional magneto-optical trap as a source for cold strontium atoms. *Physical Review A*, 96(5):053415, November 2017. Publisher: American Physical Society.

[62] Wolfgang Petrich, Michael H. Anderson, Jason R. Ensher, and Eric A. Cornell. Behavior of atoms in a compressed magneto-optical trap. *JOSA B*, 11(8):1332–1335, August 1994. Publisher: Optica Publishing Group.

[63] Wolfgang Ketterle, Kendall B. Davis, Michael A. Joffe, Alex Martin, and David E. Pritchard. High densities of cold atoms in a *dark* spontaneous-force optical trap. *Physical Review Letters*, 70(15):2253–2256, April 1993.

[64] Magnus Haw, Nathan Evetts, Will Gunton, Janelle Van Dongen, James L. Booth, and Kirk W. Madison. Magneto-optical trap loading rate dependence on trap depth and vapor density. *JOSA B*, 29(3):475–483, March 2012. Publisher: Optica Publishing Group.

[65] Saptarishi Chaudhuri, Sanjukta Roy, and C. S. Unnikrishnan. Realization of an intense cold Rb atomic beam based on a two-dimensional magneto-optical trap: Experiments and comparison with simulations. *Physical Review A*, 74(2):023406, August 2006. Publisher: American Physical Society.

[66] Daryl W. Preston. Doppler-free saturated absorption: Laser spectroscopy. *American Journal of Physics*, 64(11):1432–1436, November 1996.

[67] N. V. Vitanov, B. W. Shore, L. Yatsenko, K. Böhmer, T. Halfmann, T. Rickes, and K. Bergmann. Power broadening revisited: theory and experiment. *Optics Communications*, 199(1):117–126, November 2001.

[68] S. R. Muniz, K. M. F. Magalhães, Ph. W. Courteille, M. A. Perez, L. G. Marcassa, and V. S. Bagnato. Measurements of capture velocity in a magneto-optical trap for a broad range of light intensities. *Physical Review A*, 65(1):015402, December 2001. Publisher: American Physical Society.

[69] H.J. Metcalf and P. van der Straten. *Laser Cooling and Trapping*. Graduate Texts in Contemporary Physics. Springer New York, 2012.

[70] Sébastien Bourdeauducq, Robert Jördens, Peter Zotov, Joe Britton, Daniel Slichter, David Leibrandt, David Allcock, Aaron Hankin, Florent Kermarrec, Yann Sionneau, Raghavendra Srinivas, Ting Rei Tan, and Justin Bohnet. ARTIQ 1.0, May 2016.

[71] Grzegorz Kasprowicz, Paweł Kulik, Michal Gaska, Tomasz Przywozki, Krzysztof Pozniak, Jakub Jarosinski, Joseph W. Britton, Thomas Harty, Chris Balance, Weida Zhang, David Nadlinger, Daniel Slichter, David Allcock, Sébastien Bourdeauducq, Robert Jördens, and Krzysztof Pozniak. ARTIQ and Sinara: Open Software and Hardware Stacks for Quantum Physics. In *OSA Quantum 2.0 Conference*, page QTu8B.14, Washington, DC, 2020. Optica Publishing Group.

[72] Haotian Liu, Shuai Peng, Bolong Jiao, Jiaming Li, and Le Luo. Ultra-low noise bipolar current source for ultracold atom magnetic system. *Review of Scientific Instruments*, 94(5):053201, May 2023.

[73] AA OPTO-ELECTRONIC. MT80-Ax-xx – MT80-BxAx-xx Datasheet.

[74] Daniel Mccarron. A Guide to Acousto-Optic Modulators.

[75] Daniel Barredo, Vincent Lienhard, Sylvain de Léséleuc, Thierry Lahaye, and Antoine Browaeys. Synthetic three-dimensional atomic structures assembled atom by atom. *Nature*, 561(7721):79–82, September 2018.

[76] Sven Jandura and Guido Pupillo. Time-Optimal Two- and Three-Qubit Gates for Rydberg Atoms. *Quantum*, 6:712, May 2022.

[77] Pedro Sales Rodriguez, John M. Robinson, Paul Niklas Jepsen, Zhiyang He, Casey Duckering, Chen Zhao, Kai-Hsin Wu, Joseph Campo, Kevin Bagnall, Minho Kwon, Thomas Karolyshyn, Phillip Weinberg, Madelyn Cain, Simon J. Evered, Alexandra A.

Geim, Marcin Kalinowski, Sophie H. Li, Tom Manovitz, Jesse Amato-Grill, James I. Basham, Liane Bernstein, Boris Braverman, Alexei Bylinskii, Adam Choukri, Robert J. DeAngelo, Fang Fang, Connor Fieweger, Paige Frederick, David Haines, Majd Hamdan, Julian Hammett, Ning Hsu, Ming-Guang Hu, Florian Huber, Ningyuan Jia, Dhruv Kedar, Milan Kornjača, Fangli Liu, John Long, Jonathan Lopatin, Pedro L. S. Lopes, Xiu-Zhe Luo, Tommaso Macrì, Ognjen Marković, Luis A. Martínez-Martínez, Xianmei Meng, Stefan Ostermann, Evgeny Ostroumov, David Paquette, Zexuan Qiang, Vadim Shofman, Anshuman Singh, Manuj Singh, Nandan Sinha, Henry Thoreen, Noel Wan, Yiping Wang, Daniel Waxman-Lenz, Tak Wong, Jonathan Wurtz, Andrii Zhdanov, Laurent Zheng, Markus Greiner, Alexander Keesling, Nathan Gemelke, Vladan Vuletić, Takuya Kitagawa, Sheng-Tao Wang, Dolev Bluvstein, Mikhail D. Lukin, Alexander Lukin, Hengyun Zhou, and Sergio H. Cantú. Experimental demonstration of logical magic state distillation. *Nature*, 645(8081):620–625, September 2025. Publisher: Nature Publishing Group.

[78] Laura Pecorari, Sven Jandura, Gavin K. Brennen, and Guido Pupillo. High-rate quantum LDPC codes for long-range-connected neutral atom registers. *Nature Communications*, 16(1):1111, January 2025. Publisher: Nature Publishing Group.